

Nucleosynthesis of Zinc and Iron-Peak Elements in Pop III Type II Supernovae: Comparison with Abundances of Very Metal-Poor Halo Stars

HIDEYUKI UMEDA AND KEN'ICHI NOMOTO

Research Center for the Early Universe and Department of Astronomy, School of Science, University of Tokyo, Hongo, Bunkyo-ku, 113-0033, Japan; umeda@astron.s.u-tokyo.ac.jp, nomoto@astron.s.u-tokyo.ac.jp

ABSTRACT

We calculate nucleosynthesis in core-collapse explosions of massive Pop III stars, and compare the results with abundances of metal-poor halo stars to constrain the parameters of Pop III supernovae. We focus on iron-peak elements and, in particular, we try to reproduce the large [Zn/Fe] observed in extremely metal-poor stars. The interesting trends of the observed ratios [Zn, Co, Mn, Cr, V/Fe] can be related to the variation of the relative mass of the complete and incomplete Si-burning regions in supernova ejecta. We find that [Zn/Fe] is larger for deeper mass-cuts, smaller neutron excess, and larger explosion energies. The large [Zn/Fe] and [O/Fe] observed in the very metal-poor halo stars suggest deep mixing of complete Si-burning material and a significant amount of fall-back in Type II supernovae. Furthermore, large explosion energies, ($E_{51} \gtrsim 2$ for $M \sim 13M_{\odot}$ and $E_{51} \gtrsim 20$ for $M \gtrsim 20M_{\odot}$), are required to reproduce [Zn/Fe] ~ 0.5 .

Subject headings: Galaxy: halo — nucleosynthesis — stars: abundances — stars: Population III — supernovae: general

1. INTRODUCTION

The abundance pattern of metal-poor stars with $[\text{Fe}/\text{H}] < -2$ provides us with very important information on the formation, evolution, and explosions of massive stars in the early evolution of the galaxy (e.g., Wheeler, Sneden & Truran 1989; Matteucci 2000). Those metal-poor stars may have been formed just a few generations after the first generation Population (Pop) III stars or they may even represent the second generation (see, e.g., Weiss, Abel & Hill 2000 for recent reviews). Their abundance patterns may be the result of the nucleosynthesis in even one single Type II supernova (SN II) (Audouze & Silk 1995; Ryan, Norris, & Beers 1996; Shigeyama & Tsujimoto 1998; Nakamura et al. 1999). Therefore comparisons with nucleosynthesis patterns in massive metal-poor stars can constrain the explosion mechanism of SNe II, which is still quite uncertain, the initial mass function (IMF) of Pop III stars, and the mixing of ejected material in the interstellar medium.

With the use of high resolution spectroscopic devices attached to large telescopes, abundance measurements of extremely metal-poor stars have become possible (e.g., McWilliam et al. 1995; Ryan et al. 1996). The number and quality of the data is expected to increase with new large telescopes such as SUBARU and VLT. The observed abundances of metal-poor halo stars show quite interesting pattern. There are significant differences between the abundance patterns in the iron-peak elements below and above $[\text{Fe}/\text{H}] \sim -2.5$. For $[\text{Fe}/\text{H}] \lesssim -2.5$, the mean values of [Cr/Fe] and [Mn/Fe] decrease toward smaller metallicity, while [Co/Fe] increases.

For Zn, early observations have shown that $[\text{Zn}/\text{Fe}] \sim 0$ for $[\text{Fe}/\text{H}] \simeq -3$ to 0 (Sneden, Gratton, & Crocker 1991). Recently Primas et al. (2000) have suggested that [Zn/Fe] increases toward smaller metallicity as seen in Figure 1, and Blake et al. (2001) has one with $[\text{Zn}/\text{Fe}] \simeq 0.6$ at $[\text{Fe}/\text{H}] = -3.3$ (see Ryan 2001).

These trends could be explained with SNe II nucleosyn-

thesis, but progenitors and supernova explosion models are significantly constrained. In SNe II, stellar material undergoes shock heating and the subsequent explosive nucleosynthesis. Iron-peak elements including Cr, Mn, Co, and Zn are produced in two distinct regions, which are characterized by the peak temperature, T_{peak} , of the shocked material. For $T_{\text{peak}} > 5 \times 10^9 \text{ K}$, material undergoes complete Si burning whose products include Co, Zn, V, and some Cr after radioactive decays. For $4 \times 10^9 \text{ K} < T_{\text{peak}} < 5 \times 10^9 \text{ K}$, incomplete Si burning takes place and its after decay products include Cr and Mn (e.g., Hashimoto, Nomoto, Shigeyama 1989; Woosley & Weaver 1995, WW95 hereafter; Arnett 1996; Thielemann, Nomoto & Hashimoto 1996).

We have discussed, using the progenitor models for solar metallicity (Nomoto & Hashimoto 1988), that decreasing trend of Mn, Cr and the increasing trend of Co toward the lower metallicity can be explained simultaneously if the mass-cut that divides the ejecta and the compact remnant tends to be deeper for more massive core-collapse SNe (Nakamura et al. 1999). This is because Mn and Cr are produced mainly in the incomplete explosive Si-burning region, while Co is produced in the deeper complete explosive Si-burning region. The mass-cut is typically located somewhere close to the border of complete and incomplete Si-burning regions. Therefore, the deeper mass-cut leads to larger Co/Mn.

As for Zn, its main production site has not been clearly identified. If it is mainly produced by s-processes, the abundance ratio [Zn/Fe] should decrease with [Fe/H]. This is not consistent with the observations of $[\text{Zn}/\text{Fe}] \sim 0$ for $[\text{Fe}/\text{H}] \simeq -2.5$ to 0 and the increase in [Zn/Fe] toward lower metallicity for $[\text{Fe}/\text{H}] \lesssim -2.5$. Another possible site of Zn production is SNe II. However, previous nucleosynthesis calculations in SNe II appears to predict decreasing Zn/Fe ratio with Fe/H (WW95; Goswami & Prantzos 2000).

Understanding the origin of the variation in [Zn/Fe] is

very important especially for studying the abundance of Damped Ly- α systems (DLAs), because $[\text{Zn}/\text{Fe}] = 0$ is usually assumed, after the work by Sneden et al. (1991), to determine their abundance pattern. In DLAs super-solar $[\text{Zn}/\text{Fe}]$ ratios have often been observed, but they have been explained that assuming dust depletion for Fe is larger than it is for Zn (e.g., Lu et al 1996; Pettini et al. 1999; Prochaska & Wolfe 1999; Molaro et al. 2000; Hou, Boissier, & Prantzos 2001) However, recent observations (Primas et al. 2000; Blake et al. 2001) suggest that the assumption $[\text{Zn}/\text{Fe}] = 0$ may not be always correct.

In this paper, using recently calculated presupernova models (Umeda & Nomoto 2001; Umeda et al. 2000) we study the nucleosynthesis pattern of iron-peak elements, focusing on Zn, in massive Pop III stars. We show that depending on stellar masses, mass-cuts, Y_e and explosion energies, large Zn/Fe can be achieved in the yields of SNe II from Pop III stars. Since Zn and Co are mainly produced in the same region, their enhancement and the reduction of Mn and Cr can be understood simultaneously with the same mechanism. We also discuss the reasons why previous models (Hashimoto et al. 1989; WW95; Thielemann et al. 1996; Nomoto et al. 1997) underproduce Zn.

2. EVOLUTION OF POP III MASSIVE STARS

The elemental abundances in metal-poor halo stars may preserve nucleosynthesis pattern of the SN explosions of Pop III stars because of the following reasons. First, the IMF of very metal-poor stars ($Z \lesssim 10^{-2} - 10^{-3} M_{\odot}$) can be similar to Pop III stars, since the dominant cooling mechanism for interstellar matter is almost the same (Böhringer & Hensler 1989). Second, the nucleosynthesis pattern in the explosions of very metal-poor Pop II stars ($Z < 10^{-2} M_{\odot}$) are similar to those of Pop III supernovae (Umeda et al. 2000). Also a single SN event is likely to induce star formation for metallicity $[\text{Fe}/\text{H}] \sim -4$ to -2 , so that the observed metal-poor stars can be the second or very early generation (Ryan et al. 1996; Shigeyama & Tsujimoto 1998; Nakamura et al. 1999).

For these reasons, we use our Pop III (metal-free) models to compare their explosive nucleosynthesis with the observed abundances of very low-metal stars. We calculate the evolution of massive Pop III stars for a mass range of $M = 13 - 30 M_{\odot}$ from pre-main sequence to Type II SN explosions. Stellar evolution is calculated with a Henyey-type stellar evolution code (Umeda et al. 2000), which runs a large nuclear reaction network with 240 isotopes to calculate detailed nucleosynthesis and nuclear energy generation. For the Pop III models we assumed no mass-loss. SN explosions are simulated with a PPM code. The detailed nucleosynthesis during the explosion is calculated by post-processing as in Nakamura et al. (2000), using a code of Hix & Thielemann (1996).

In the metal-free star evolution, CNO elements are absent during the early stage of hydrogen burning. Therefore, the CNO cycle does not operate initially and the star contracts until the central temperature rises sufficiently high for the 3α reaction to produce ^{12}C with mass fraction $\sim 10^{-10}$. Then Pop III stars undergo the CNO cycle at a much higher central temperature ($T_c \sim 1.5 \times 10^8 \text{ K}$) than metal-poor Pop II stars (e.g., Ezer, & Cameron 1971; Castellani, Chieffi, & Tornambé 1983). On the other hand,

the late core evolution and the resultant Fe core masses of Pop III stars are not significantly different from Pop II stars (e.g., WW95; Limongi, Chieffi, & Straniero 1998; Umeda et al. 2000). In Table 1, we show the “Fe”-core masses of our model defined as a region with the electron mole fraction $Y_e \leq 0.49$ for various Z and initial masses. The distribution of Y_e in the inner core at the beginning of collapse ($\rho_c \sim 3 \times 10^{10} \text{ g cm}^{-3}$) is shown in Figure 2.

One of the uncertainties in the calculations of stellar evolution is the treatment of convection. Here we use the models assuming relatively slow convective mixing ($f_k = 0.05$ in the parameter described in Umeda et al. 2000). Larger f_k leads to stronger mixing of nuclear fuel, thus resulting in stronger convective shell-burning, which leads to less compact core and less massive remnants. With the choice $f_k = 0.05$, the baryon masses of the compact remnants are 1.55 and $1.67 M_{\odot}$ for the 13 and $15 M_{\odot}$ solar metallicity stars, respectively. A more detailed description of the presupernova models and parameter dependences are given elsewhere (Umeda & Nomoto 2001; also Umeda et al. 2000).

3. SYNTHESIS OF ZINC IN POP III SUPERNOVAE

We briefly summarize general nucleosynthesis of Pop III supernovae obtained in Umeda et al. (2000). The mass fraction ratio of odd and even Z elements (e.g., Al/Mg), and the inverse ratio of α -elements and their isotopes (e.g. $^{13}\text{C}/^{12}\text{C}$) decrease for lower metallicity. However, the former ratios almost saturate for low metallicity ($Z < \sim 10^{-3}$) and the latter ones are difficult to observe. Therefore, the differences in the nucleosynthesis pattern between the very metal-poor Pop II and Pop III stars are difficult to observe. The abundance ratio among the even Z elements are almost independent of the metallicity.

Dependencies on the mass and explosion energy are more important. These results suggest that in discussing the abundance pattern of very metal-poor stars, effects other than the metallicity are likely to be more important, which is consistent with WW95. In the following, we discuss the dependence of the production of Zn and other iron-peak elements on the mass, mass-cut, and explosion energy separately.

3.1. Dependence on Mass-Cut (M_{cut})

Here we discuss the dependence of yields on the mass-cut, $M_r = M_{\text{cut}}$. The explosion energy is assumed to be $E_{51} = E_{\text{exp}}/(10^{51} \text{ erg}) = 1$. The abundance distribution after explosion for 13 and $15 M_{\odot}$ models is shown in Figure 3. Here the upper bounds of the complete Si-burning region and the incomplete Si-burning region are defined by $X(^{56}\text{Ni}) = 10^{-3}$ and $X(^{28}\text{Si}) = 10^{-4}$, respectively. The lines labeled by Cr, Mn, Co and Zn actually indicate unstable ^{52}Fe , ^{55}Co , ^{59}Cu , and ^{64}Ge , respectively, which eventually decay into the labeled elements.

In the ejecta, the mass fraction of the complete Si burning products is larger if the mass-cut is deeper (i.e., M_{cut} is smaller). Mn and Cr are produced mainly in the incomplete explosive Si-burning region, while Co and Zn are mainly produced in the deeper complete explosive Si-burning region. Therefore, if the mass-cut is deeper, the abundance ratios Co/Fe and Zn/Fe increase, while the ratios Mn/Fe and Cr/Fe decrease as seen in Figure 4.

Figure 4 shows that larger [Zn, Co/Fe] and smaller [Mn/Fe] can be achieved simultaneously for a smaller M_{cut} . In the $13 M_{\odot}$ model for $M_{\text{cut}} \sim 1.55 M_{\odot}$, for example, [Zn/Fe] is large enough to be consistent with the observed ratio [Zn/Fe] ~ 0.1 for [Fe/H] $\gtrsim -2$ stars. More massive stars can also yield [Zn/Fe] $\gtrsim 0$ if the mass-cut is deep enough. The observed large ratio [Zn/Fe] ~ 0.5 in very metal-poor stars only can be achieved with the combination of deep mass-cut and large explosion energy (§3.4).

Another effect of the mass cut on the yield is the ^{56}Ni mass in the ejecta $M(^{56}\text{Ni})$, which is larger for smaller M_{cut} as shown in Figure 4. Ejection of the large amount of radioactive ^{56}Ni has actually been seen in such bright supernovae as SNe 1997ef and 1998bw (e.g., Nomoto et al. 2000). We note that for $M \gtrsim 15 M_{\odot}$, the $M(^{56}\text{Ni})$ required to get [Zn/Fe] ~ 0.5 appears to be too large to be compatible with observations of [O/Fe] $\sim 0 - 0.5$ in metal-poor stars. However, if fall-back of enough amount of iron-peak elements occurs after mixing, $M(^{56}\text{Ni})$ can be smaller without changing the [Zn/Fe] ratio, as will be discussed in §3.5.

3.2. Dependence on Stellar Mass

Figure 4 shows that the relation between [X/Fe] and $M(^{56}\text{Ni})$ is sensitive to the progenitor mass. To understand this behavior, we summarize in Table 2 the location of the incomplete Si-burning region in M_r and $M(^{56}\text{Ni})$ contained in this region for several models. The thickness in mass of the incomplete Si-burning region (and thus $M(^{56}\text{Ni})$ there) is larger for larger progenitor masses. Suppose that all SNe II eject the same amount of ^{56}Ni . Then the fraction of complete Si burning products is larger for less massive stars because the incomplete Si-burning region is thinner. This is why the $13 M_{\odot}$ model yields larger [Zn, Co/Fe] than more massive models if for example $M(^{56}\text{Ni}) = 0.07 M_{\odot}$ (Fig. 4). Models heavier than $15 M_{\odot}$ are consistent with very metal-poor star data if M_{cut} is small (i.e., $M(^{56}\text{Ni})$ is large).

The *maximum* values of [X/Fe] as a function of M_{cut} also depend on the stellar mass because of the different density - temperature histories and Y_e distribution of the progenitors. There is a tendency that the *maximum* [Zn, Co/Fe] decreases with increasing stellar mass. One of the reasons for this trend is that more massive stars have thicker incomplete Si-burning region, and thus deeper material must be ejected to make [Zn, Co/Fe] large. As discussed in the next subsection, in the deeper regions Y_e is typically smaller, which leads also to smaller Zn and Co mass fractions. On the other hand, there is no clear mass dependence for [Mn, Cr/Fe].

3.3. Dependence on Y_e

In order to see the dependence on Y_e , in Figure 5 we compare the post-explosive abundance distribution of the $25 M_{\odot}$ ($E_{51}=1$) models. The left panel shows the original model, whose Y_e distribution is enlarged in Figure 6. In the right panel Y_e is modified to be 0.5 at $M_r \leq 2.5 M_{\odot}$. As shown in these figures, Zn and Co abundances are very sensitive to Y_e . If Y_e decreases below $Y_e \simeq 0.4998$, the Zn abundance becomes significantly smaller, because Zn

is the decay product of the symmetric species ^{64}Ge . The dependence of the Co abundance on Y_e is not monotonic but rather complicated, though the Co abundance is larger in the $Y_e = 0.5$ model of this example. (X(Co) is relatively large for $Y_e = 0.5$. It decreases once for lower Y_e but it increases again toward $Y_e \simeq 0.49$.) Previous progenitor models in Nomoto & Hashimoto (1988) have much lower Y_e than our current models in the complete Si-burning region because of the different initial metallicity and treatment of convection, and this is the main reason why previous models significantly underproduce Zn even for the $13 M_{\odot}$ model.

In our present progenitor models (as well as in Nomoto & Hashimoto 1988), we have applied electron-capture rates by Fuller, Fowler, & Newman (1980, 1982). The use of the recent rates by Langanke & Martínez-Pinedo (2000), which are lower than Fuller et al. (1980, 1982) would lead to larger Y_e (Heger et al. 2000). Mezzacappa et al. (2000) and Rampp & Janka (2000) have recently performed simulations of SNe II with full Boltzmann neutrino transports, and they have shown that Y_e in the deep layers may be enhanced up to around 0.5 by neutrino processes. If this is the case, Zn production may be significantly enhanced even for the progenitor models of Nomoto & Hashimoto (1988). We should note that X(Zn) can be large even if $Y_e \lesssim 0.4995$ for energetic explosion as will be discussed in the next subsection.

3.4. Dependence on Explosion Energy

Recently we had some evidences that at least some core collapse SNe explode with large explosion energy, which may be called “Hypernovae” (e.g., Nomoto et al. 2000). These SNe likely originate from relatively massive SNe ($M \gtrsim 25 M_{\odot}$).

In Figure 7 we show nucleosynthesis in the $25 M_{\odot}$ star with the explosion energy of 10^{52} erg. (In this figure, the distribution of ^{51}Mn which decays into V is also shown; V is mostly produced in the complete Si-burning region.) By comparing with Figure 5, we find that for larger explosion energies, the boundaries of both the complete and incomplete Si burning regions move outward in mass coordinates. We also find that for a larger explosion energy the incomplete Si burning region is thicker in mass, thus containing a larger amount of ^{56}Ni (Table 2).

Therefore, hypernova explosions, which eject a large amount of complete Si burning products, also produce a larger amount of ^{56}Ni than ordinary SNe II, unless significant fall-back takes place after mixing (see §3.5). This is seen in Figure 8, which shows that [Zn/Fe] $\gtrsim 0.3$ only for $M(^{56}\text{Ni}) \gtrsim 0.7 M_{\odot}$ (i.e., bright supernovae).

The explosion energy also affects the local mass-fraction of elements. For more energetic explosions, the temperature during the explosion is higher for the same density (Nakamura et al. 2000). Figures 5 and 7 show that for a higher energy X(Co) and X(Zn) is enhanced in complete-Si burning and X(Mn) is reduced in incomplete-Si burning. X(Cr) in incomplete-Si burning is almost unchanged.

In order to show the parameter dependences of X(Zn), we plot in Figure 9 the density - temperature track during explosive complete Si-burning for four representative cases following the maximum temperature (open circles). The parameters of the four models and the mass fractions

of ^{56}Ni and Zn are summarized in Table 3. Cases B & D produce large $X(\text{Zn})$, while A & C are the cases with smaller $X(\text{Zn})$. Case C' is the same as case C except for the modifications of Y_e . The general trend is that $X(\text{Zn})$ is larger if Y_e is closer to 0.5 and an explosion is more energetic to produce larger T^3/ρ . Cases A and C have low $X(\text{Zn})$ because of relatively low Y_e . Case C' has the same density - temperature history as case C, but it yields larger $X(\text{Zn})$ due to the larger Y_e . Case D has the same Y_e as case C, but it yields larger $X(\text{Zn})$ due to larger T^3/ρ . Case B yields large $X(\text{Zn})$ because of the relatively large Y_e and T^3/ρ .

In Figures 10 and 11, we show the time evolution of density, temperature, T^3/ρ and mass fraction ratios of some elements that are relevant to Zn synthesis for cases C (C') and D. These figures show that for larger T^3/ρ the mass fraction of ^4He is larger and thus the α -rich effect is enhanced. Then the larger fractions of ^{56}Ni and ^{60}Zn are converted to ^{64}Ge , which enhances the Zn mass fraction.

We note that the trend that large E gives high T^3/ρ during α -rich freezeout can be further enhanced in non-spherical explosions. This is because the shock in the jet-direction is stronger than the shock in the spherical model with the same E (e.g., Maeda et al. 2000; Nagataki et al. 1997).

3.5. Mixing and Fall-back

We have shown that large $[\text{Zn}, \text{Co}/\text{Fe}]$ and small $[\text{Mn}, \text{Cr}/\text{Fe}]$ can be obtained simultaneously if M_{cut} is sufficiently small. However, the ejected ^{56}Ni mass is larger for smaller M_{cut} , and $M(^{56}\text{Ni})$ required to get $[\text{Zn}/\text{Fe}] \sim 0.5$ appears to be too large to be compatible with observations $[\text{O}/\text{Fe}] \sim 0 - 0.5$.

Here we consider a possible process that realizes effectively smaller mass-cuts without changing the ^{56}Ni mass. In SNe II, when the rapidly expanding core hits the H and He envelopes, a reverse shock forms and decelerates core expansion. The deceleration induces Rayleigh-Taylor instabilities at the composition interfaces of H/He, He/C+O, and O/Si as has been found in SN 1987A (e.g., Ebisuzaki, Shigeyama, & Nomoto 1989; Arnett et al. 1989). Therefore, mixing can take place between the complete and incomplete Si burning regions according to the recent two dimensional numerical simulations (Kifonidis et al. 2000; Kifonidis 2001). The reverse shock can further induce matter fall-back onto the compact remnant (e.g., Chevalier 1989).

Based on these earlier findings, we propose that the following “mixing fall-back” process takes place in most SNe II.

(1) Burned material is uniformly mixed between the “initial” mass-cut ($M_{\text{cut}}(i)$) and the top of the incomplete Si-burning region at $M_r = M_{\text{Si}}$. Then $[\text{Zn}/\text{Fe}]$ in the mixed region becomes as large as ~ 0.5 .

(2) Afterwards the mixed materials below $M_{\text{cut}}(f)$ ($> M_{\text{cut}}(i)$) fall-back onto the compact remnant, and $M_{\text{cut}}(f)$ becomes the final mass-cut. Then $M(^{56}\text{Ni})$ becomes smaller while the mass ratios ($\text{Zn}, \text{Co}, \text{Mn}/\text{Fe}$) remain the same compared with the values determined by $M_{\text{cut}}(i)$ in Figures 4 and 8.

The adopted model parameters of SNe II ($M, E, M_{\text{cut}}(i), M_{\text{cut}}(f)$), M_{Si} , and the resultant $[\text{O}/\text{Fe}]$

and $[\text{Zn}/\text{Fe}]$ are summarized in Table 4. Here the initial mass cuts $M_{\text{cut}}(i)$ are chosen to give maximum $[\text{Zn}/\text{Fe}]$. For $M_{\text{cut}}(f)$ we consider two cases that give $[\text{O}/\text{Fe}] \sim 0.3 - 0.5$ and 0.0, respectively (for $M \geq 20M_\odot$). Here $M_{\text{cut}}(f)$ is chosen to eject no less than $0.07M_\odot$ of ^{56}Ni . Note that the ratio $[\text{Zn}/\text{Fe}]$ is independent of $M_{\text{cut}}(f)$. Note also that larger E leads to larger $[\text{Zn}/\text{Fe}]$ as discussed in §3.4.

This “mixing and fall-back” effect may also be effectively realized in non-spherical explosions accompanying energetic jets (e.g., Maeda et al. 2000; Khoklov et al. 1999; Nagataki et al. 1997). Compared with the spherical model with the same $M_{\text{cut}}(i)$ and E , the shock is stronger (weaker) and thus temperatures are higher (lower) in the jet (equatorial) direction. As a result, a larger amount of complete Si-burning products are ejected in the jet direction, while only incomplete Si-burning products are ejected in the equatorial direction. In total, complete Si-burning elements can be enhanced (Maeda 2001).

4. SUMMARY AND DISCUSSION

We have calculated nucleosynthesis in massive Pop III stars using our recent metal-free progenitor models, and compared the results with the abundances of metal-poor halo stars to constrain the structures and explosion models of Pop III stars. In the present work, we have focussed on iron-peak elements and, in particular, explored the parameter ranges ($M_{\text{cut}}(i)$, Y_e , M , and E) to reproduce $[\text{Zn}/\text{F}] \sim 0.5$ observed in extremely metal-poor stars. Our main results are summarized as follows.

1) The interesting trends of the observed ratios $[(\text{Zn}, \text{Co}, \text{Mn}, \text{Cr})/\text{Fe}]$ can be understood in terms of the variation of the mass ratio between the complete Si burning region and the incomplete Si burning region. The large Zn and Co abundances observed in very metal-poor stars are obtained if the mass-cut is deep enough (i.e., if $M_{\text{cut}}(i)$ is small enough in Figures 4 and 8), or equivalently if deep material from complete Si-burning region is ejected by mixing or aspherical effects (§3.1). Vanadium also appears to be abundant at low $[\text{Fe}/\text{H}]$ (e.g., Goswami & Prantzos 2000). Since V is also produced mainly in the complete Si-burning region (Fig. 7), this trend can be explained in the same way as those of Zn and Co.

2) The mass of the incomplete Si burning region is sensitive to the progenitor mass M , being smaller for smaller M . Thus $[\text{Zn}/\text{Fe}]$ tends to be larger for less massive stars for the same E (§3.2).

3) The production of Zn and Co is sensitive to the value of Y_e , being larger as Y_e is closer to 0.5, especially for the case of a normal explosion energy ($E_{51} \sim 1$) (§3.3).

4) A large explosion energy E results in the enhancement of the local mass fractions of Zn and Co, while Cr and Mn are not enhanced (Fig. 8). This is because larger E produces larger entropy and thus more α -rich environment for α -rich freeze-out (§3.4).

5) To be consistent with the observed $[\text{O}/\text{Fe}] \sim 0 - 0.5$ as well as with $[\text{Zn}/\text{Fe}] \sim 0.5$ in metal-poor stars, we propose that the “mixing and fall-back” process or aspherical effects are significant in the explosion of relatively massive stars (§3.5).

The dependence of $[\text{Zn}/\text{Fe}]$ on M and E is summarized in Figures 12 and 13 as follows.

a) In Figure 12, we compare the [Zn/Fe] ratios in our $E_{51} = 1$ models with previous models for various progenitor masses M . The [Zn/Fe] ratio depends also on $M_{\text{cut}}(i)$, and our values in Figure 12 correspond to the maximum values for $E_{51} = 1$. The difference in Y_e is the primary reason why Zn production is much smaller when previous progenitor models by Nomoto & Hashimoto (1998) are used (Thielemann et al. 1996). (Note that, for hypernova-like explosion energies, Zn is abundantly produced even if Y_e is smaller while Zn production is suppressed otherwise.) Differences from WW95 may mostly stem from the differences in $M_{\text{cut}}(i)$. Limongi, Stranciero & Chieffi (2000) has also shown their yields for some $Z = 0$ models. Probably because of lower Y_e , their Zn yields are smaller than ours by a factor of more than 10^5 , thus being out of range in Figure 12.

b) In Figure 13, [Zn/Fe] is shown as a function of M and E , where the plotted ratios correspond to the maximum values for given E . We have found that models with $E_{51} = 1$ do not produce sufficiently large [Zn/Fe]. To be compatible with the observations of [Zn/Fe] ~ 0.5 , the explosion energy must be much larger, i.e., $E_{51} \gtrsim 2$ for $M \sim 13M_\odot$ and $E_{51} \gtrsim 20$ for $M \gtrsim 20M_\odot$.

Observationally, the requirement of the large E might suggest that large M stars are responsible for large [Zn/Fe], because E and M can be constrained from the observed brightness and light curve shape of supernovae as follows. [The uncertainties in theoretical models for gravitational collapse are still too large to determine E (e.g., Mezzacappa et al. 2000; Rampp and Janka 2000).] The recent supernovae 1987A, 1993J, and 1994I indicate that the progenitors of these normal SNe are $13 - 20 M_\odot$ stars and $E_{51} \sim 1 - 1.5$ (Nomoto et al. 1993, 1994; Shigeyama et al. 1994; Blinnikov et al. 2000). On the other hand, the masses of the progenitors of hypernovae with $E_{51} > 10$ (SNe 1998bw, 1997ef, and 1997cy) are estimated to be $M \gtrsim 25M_\odot$ (Nomoto et al. 2000; Iwamoto et al. 1998, 2000; Woosley et al. 1999; Turatto et al. 2000). This could be related to the stellar mass dependence of the explosion mechanisms and the formation of compact remnant, i.e., less massive stars form neutron stars, while more massive stars tend to form black holes.

To explain the observed relation between [Zn/Fe] and [Fe/H], we further need to know how M and E of supernovae and [Fe/H] of metal-poor halo stars are related. In the early galactic epoch when the galaxy is not yet chemically well-mixed, [Fe/H] may well be determined by mostly a single SN event (Audouze & Silk 1995). The formation of metal-poor stars is supposed to be driven by a supernova shock, so that [Fe/H] is determined by the ejected Fe mass and the amount of circumstellar hydrogen swept-up by the shock wave (Ryan et al. 1996).

Explosions with the following two combinations of M and E can be responsible for the formation of stars with very small [Fe/H]:

i) Energetic explosions of massive stars ($M \gtrsim 25M_\odot$): For these massive progenitors, the supernova shock wave tends to propagate further out because of the large explosion energy and large Strömgren sphere of the progenitors (Nakamura et al. 1999). The effect of E may be important since the hydrogen mass swept up by the supernova shock is roughly proportional to E (e.g., Ryan et al 1996;

Shigeyama & Tsujimoto 1998).

ii) Normal supernova explosions of less massive stars ($M \sim 13M_\odot$): These supernovae are assumed to eject a rather small mass of Fe (Shigeyama & Tsujimoto 1998), and most SNe are assumed to explode with normal E irrespective of M .

The above relations lead to the following two possible scenarios to explain [Zn/Fe] ~ 0.5 observed in metal-poor stars.

i) Hypernova-like explosions of massive stars ($M \gtrsim 25M_\odot$) with $E_{51} > 10$: Contribution of highly asymmetric explosions in these stars may also be important. The question is what fraction of such massive stars explode as hypernovae; the IMF-integrated yields must be consistent with [Zn/Fe] ~ 0 at [Fe/H] $\gtrsim -2.5$.

ii) Explosion of less massive stars ($M \lesssim 13M_\odot$) with $E_{51} \gtrsim 2$ or a large asymmetry: This scenario, after integration over the IMF, can reproduce the observed abundance pattern for [Fe/H] $\gtrsim -2$ (Tsujimoto & Shigeyama 1998). However, the Fe yield has to be very small in order to satisfy the observed [O/Fe] value ($\gtrsim 0.5$) for the metal-poor stars. For example, the ^{56}Ni mass yield of our $13M_\odot$ model has to be less than $0.006M_\odot$, which appears to be inconsistent with the nearby SNe II observations.

It seems that the [O/Fe] ratio of metal-poor stars and the E - M relations from supernova observations favor the massive energetic explosion scenario for enhanced [Zn/Fe]. However, we need to construct detailed galactic chemical evolution models to distinguish between the two scenarios for [Zn/Fe]. For that purpose, in Figures 14-16, we show the overall abundance pattern in the ejecta (after radioactive decays) for the models which yield [Zn/Fe] = 0.3 - 0.6 as a result of the “mixing and fall-back” process (except for the $13 M_\odot$ model). The mass-cuts are chosen to eject $0.07M_\odot$ ^{56}Ni for 13 and $15 M_\odot$, and to realize [O/Fe]=0 for $M \gtrsim 25M_\odot$. The yields are also listed in Tables 5-13. Here large [O/Fe] ($\sim 0.3 - 0.5$) is assumed for $M \gtrsim 20M_\odot$ to reproduce the majority of the observed abundance pattern.

We note that our Mn yields are roughly factor 10 smaller than in Nomoto et al. (1997) and Nakamura et al. (1999), and Cr is slightly over-produced. Main source of the differences is that Y_e in the incomplete Si-burning region of our models are larger than that of previous models. If Y_e in the incomplete Si-burning layers is slightly reduced from 0.49996 to 0.49977, for example, Mn yield is enhanced by a factor 10 and Cr yield is slightly reduced. Smaller Y_e leads to smaller Zn mass fraction. For $Y_e = 0.49977$, however, the produced amount of Zn is almost the same as in our current models as far as the explosions are energetic.

Our Co yields as in all previous works (Nomoto et al. 1997; WW95; Nakamura et al. 1999) are at least factor of 3-5 smaller than the observed ones. One of the reasons might be that Co has an odd Z number and its abundance is sensitive to uncertain reaction rates involving proton and neutrons. On the other hand, Zn production is mostly determined by less uncertain reaction rates involving α -particles.

One may wonder whether the abundance anomaly of iron-peak elements discussed in this paper may be related to the peculiar IMF of Pop III stars. It is quite likely that the IMF of Pop III stars is different from that of Pop I

and II stars, and that more massive stars are abundant for Pop III (e.g., Nakamura & Umemura 1999; Omukai & Nishi 1999; Bromm, Coppi & Larson 1999). They have discussed that the IMF of Pop III and very low metal stars may have a peak at even larger masses, around $\sim (1\text{-few}) \times 100M_{\odot}$. If $M \lesssim 130M_{\odot}$, then these stars are likely to form black holes either without explosion or with energetic explosions. The nucleosynthesis of the latter case may not be so different from the models considered here. This might favor the scenario that invokes the hypernova-like explosions for large [Zn/Fe].

If stars are even more massive than $\sim 150M_{\odot}$, these become pair instability SNe and their nucleosynthesis is different from the ones considered here (Barkat, Rakavy & Sack 1967). These SNe are discussed elsewhere, but these stars are unlikely to produce a sufficiently large Zn/Fe ratio.

In this paper, we have shown that such a large Zn abundance as [Zn/Fe] ~ 0.5 observed in metal-poor stars can be realized in certain supernova models. This implies that

the assumption of [Zn/Fe] ~ 0 usually adopted in the DLA abundance analyses may not be well justified. Rather [Zn/Fe] may provide important information on the IMF and/or the age of the DLA systems.

We have considered only a few elements to constrain the nucleosynthesis of Pop III stars, because their trends are most clear. Data for other elements show less clear trends or currently have relatively large error bars. However, additional information will be very useful. For example, [S/Fe] and [C/O] may be important to distinguish the scenarios of $M \lesssim 13M_{\odot}$ and $M \gtrsim 20M_{\odot}$. Also mass-cut independent ratios [Ca, S, Si/Mg] will be important to constrain the explosion energies of SNe.

We would like to thank S. Ryan, C. Kobayashi, T. Nakamura, K. Maeda, M. Shirouzu, and K. Kifonidis for useful discussion. This work has been supported in part by the grant-in-Aid for COE Scientific Research (07CE2002, 12640233) of the Ministry of Education, Science, Culture, and Sports in Japan.

REFERENCES

Arnett, W.D. 1996, *Supernovae and Nucleosynthesis* (New Jersey: Princeton University Press)

Arnett, W.D., Bahcall, J.N., Kirshner, R.P., Woosley, S.E. 1989, *ARA&A*, 27, 629

Audouze, J., & Silk, J. 1995, *ApJ*, 451, L49

Barkat, Z., Rakavy, G., & Sack, N., 1967, *Phys. Rev. Letters*, 18, 379

Blake, L.A.J., Ryan S.G., Norris, J.E., & Beers, T.C. 2001, *Nucl.Phys.A*, in press

Blinnikov, S., Lundqvist, P., Bartunov, O., Nomoto, K., & Iwamoto, K., 2000, *ApJ*, 532

Böhringer, H., & Hensler, G. 1989, *A&A*, 215, 147

Bromm, V., Coppi, P.S., & Larson, R. B. 1999, *ApJ*, 527, L5

Castellani, V., Chieffi A., & Tornambé A. 1983, *ApJ*, 272, 249

Chevalier, R.A. 1989, *ApJ*, 346, 847

Ebisuzaki, T., Shigeyama, T., & Nomoto, K. 1989, *ApJ*, 344, 65

Ezer, D., & Cameron, A.G.W. 1971, *Astrophys. Space Sci.*, 14, 399

Fuller, G.M., Fowler, W.A., & Newman, M.J., 1980, *ApJS*, 42 447 — 1982, *ApJS*, 48, 279

Goswami, A., & Prantzos, N. 2000, *A&A*, 359, 191

Heger, A., Woosley, S. E., Martínez-Pinedo, G., & Langanke, K. 2000, *ApJ*, submitted (astro-ph/0011507)

Hashimoto, M., Nomoto, K., Shigeyama, T. 1989, *A&A*, 210, L5

Hix, W. R. & Thielemann, F.-K. 1996, *ApJ*, 460, 869

Hou, J.L., Boissier, S., & Prantzos, N. 2001, *A&A*, in press (astro-ph/0102188)

Iwamoto, K., Mazzali, P.A., Nomoto, K., Umeda, H., et al. 1998, *Nature*, 395, 672

Iwamoto, K., Nakamura, T., Nomoto, K. et al. 2000, *ApJ*, 534, 660

Khoklov, A.M., Höflich, P.A., Oran, E.S., Wheeler, J.C., Wang, L., Chtchelkanova, A. Y. 1999, *ApJ*, 524, 107

Kifonidis, K. 2001, Ph.D. thesis, Max-Planck-Institut für Astrophysik

Kifonidis, K., Plewa, T., Janka, H-Th., & Müller, E. 2000, *ApJ*, 531, L123

Langanke, K. & Martínez-Pinedo, G. 2000, *Nucl. Phys. A*, 673, 481

Limongi, M., Chieffi, A., & Straniero, O. 1998, in *Nuclei in the Cosmos V*, ed. N. Prantzos, & S. Harissopoulos (Paris: Editions Frontières), 144

Limongi, M., Chieffi, A., & Straniero, O. 2000, *ApJS*, 129, 625

Lu, L., Sargent, W. L. W., Barlow, T. A., Churchill, C. W., & Vogt, Steven S. 1996, *ApJS*, 107, 405

Maeda, K., Nakamura, T., Nomoto, K., Mazzali, P.A., Patat, F., & Hachisu, I. 2000, *ApJ*, submitted (astro-ph/0011003)

Maeda, K. 2001, Master's thesis, University of Tokyo

Matteucci, F. 2000, *The Chemical Evolution of the Galaxy*

Mezzacappa, A., Liebendoerfer, M., Messer, O.E.B., Hix, W.R., Thielemann, F.-k., & Bruenn, S.W. 2000, *Phys. Rev. Lett.*, submitted (astro-ph/0005366)

McWilliam, A., Preston, G. W., Sneden, C., & Searle, L. 1995, *AJ*, 109, 2757

Molaro, P., Bonifacio, P., Centurion, M., D'Odorico, S., Vladilo, G., Santin, P., & Di Marcantonio, P. 2000, *ApJ*, 541, 54

Nagataki, S., Hashimoto, M., Sato, K., & Yamada, S. 1997, *ApJ*, 486, 1026

Nakamura, F., & Umemura, M. 1999, *ApJ*, 515, 239

Nakamura, T., Umeda, H., Nomoto, K., Thielemann, F.-K., & Burrows, A. 1999, *ApJ*, 517, 193

Nakamura, T., Umeda, H., Iwamoto, K., Nomoto, K., Hashimoto, M., Hix, W.R., Thielemann, F.-K. 2000, *ApJ*, submitted (astro-ph/0011184)

Nomoto, K. & Hashimoto, M. 1988, *Phys. Rep.*, 256, 173

Nomoto, K., Suzuki, T., Shigeyama, T., Kumagai, S., Yamaoka, H., & Saio, H. 1993, *Nature*, 364, 507

Nomoto, K., Yamaoka, H., Pols, O.R., van den Heuvel, E.P.J., Iwamoto, K., Kumagai, S., & Shigeyama, T. 1994, *Nature*, 371, 227

Nomoto, K., Hashimoto, M., Tsujimoto, T., Thielemann, F.-K., Kishimoto, N., Kubo, Y., & Nakasato, N. 1997, *Nucl. Phys. A* 616, 79

Nomoto, K., et al. 2000, in *Supernovae and Gamma Ray Bursts*, ed. M. Livio et al. (Cambridge: Cambridge University Press), in press (astro-ph/0003077)

Omukai, K., & Nishi, R. 1999, *ApJ*, 518, 64

Pettini, M., Ellison, S. L., Steidel, C. C., Bowen, D. V. 1999, *ApJ*, 510, 576

Primas, F., Reimers, D., Wisotzki, L., Reetz, J., Gehren, T., & Beers, T.C. 2000, in *The First Stars*, ed. A. Weiss, T. Abel, & V. Hill (Berlin: Springer), 51

Prochaska, J. X., & Wolfe, A. M. 1999, *ApJS*, 211, 369

Rampp, M., & Janka, H.-T. 2000, *ApJ*, 539, L33

Ryan, S. G., Norris, J. E., & Beers, T. C. 1996, *ApJ*, 471, 254

Ryan, S. G. 2001, in *The Influence of Binaries on Stellar Populations Studies*, ed. D. Vanbeveren (Kluwer), in press

Shigeyama, T., Suzuki, T., Kumagai, S., Nomoto, K., Saio, H., & Yamaoka, H. 1994, *ApJ*, 420, 341

Shigeyama, T., & Tsujimoto, T. 1998, *ApJ*, 507, L135

Sneden, C., Gratton, R.G., & Crocker, D.A. 1991, *A&A*, 246, 354

Thielemann, F.-K., Nomoto, K., & Hashimoto, M. 1996, *ApJ*, 460, 408

Tsujimoto, T., & Shigeyama, T. 1998, *ApJ*, 508, L151

Turatto, M., Suzuki, T., Mazzali, P.A., Benetti, S., Cappellaro, E., Nomoto, K., Nakamura, T., Young, T., & Patat, F. 2000, *ApJ*, 534, L57

Umeda, H., Nomoto, K., & Nakamura, T. 2000, in *The First Stars*, ed. A. Weiss, T. Abel, & V. Hill (Berlin: Springer), 150 (astro-ph/9912248)

Umeda, H., & Nomoto, K. 2001, in preparation

Wheeler, J.C., Sneden, C., & Truran, J.W. 1989, *ARA&A*, 27, 279

Weiss, A., Abel, T., & Hill, V. 2000, ed. *The First Stars* (Berlin: Springer)

Woosley, S.E., Eastman, R.G., & Schmidt, B.P. 1999, *ApJ*, 516, 788

Woosley, S.E., & Weaver, T.A. 1995, *ApJS*, 101, 181 (WW95)

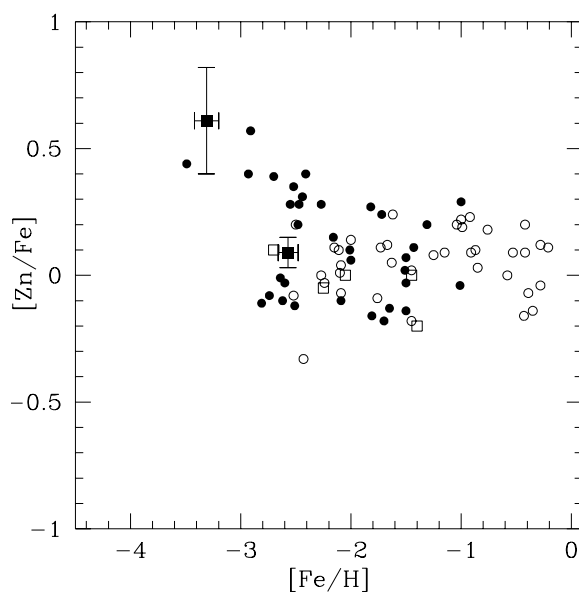


FIG. 1.— Observed abundance ratios of $[Zn/Fe]$. These data are taken from Primas et al. (2000) (filled circles), Blake et al. (2001) (filled square) and from Sneden et al. (1991) (others).

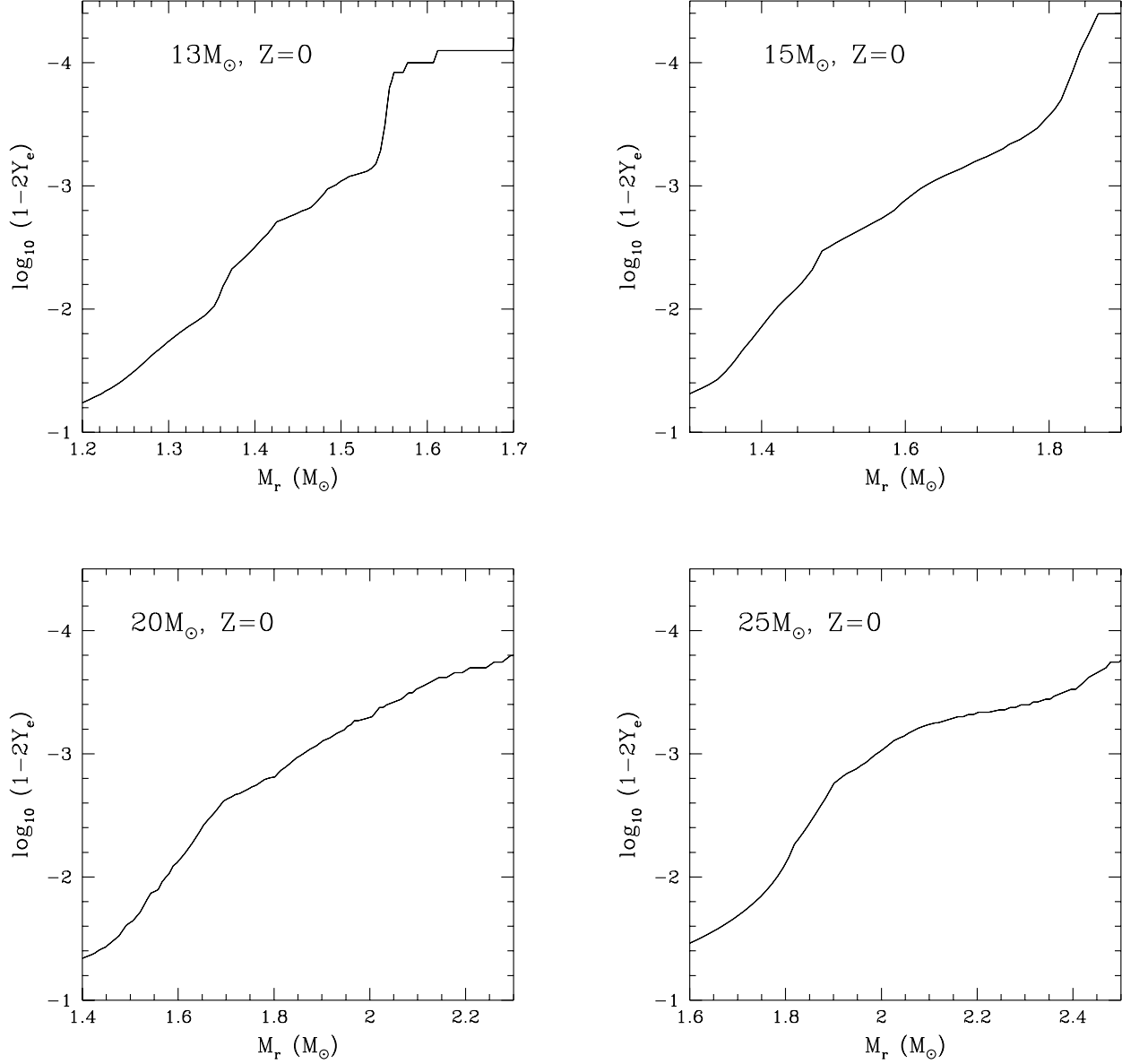


FIG. 2.— Y_e distribution of the Pop III pre-supernova progenitor models with $13 - 25M_\odot$.

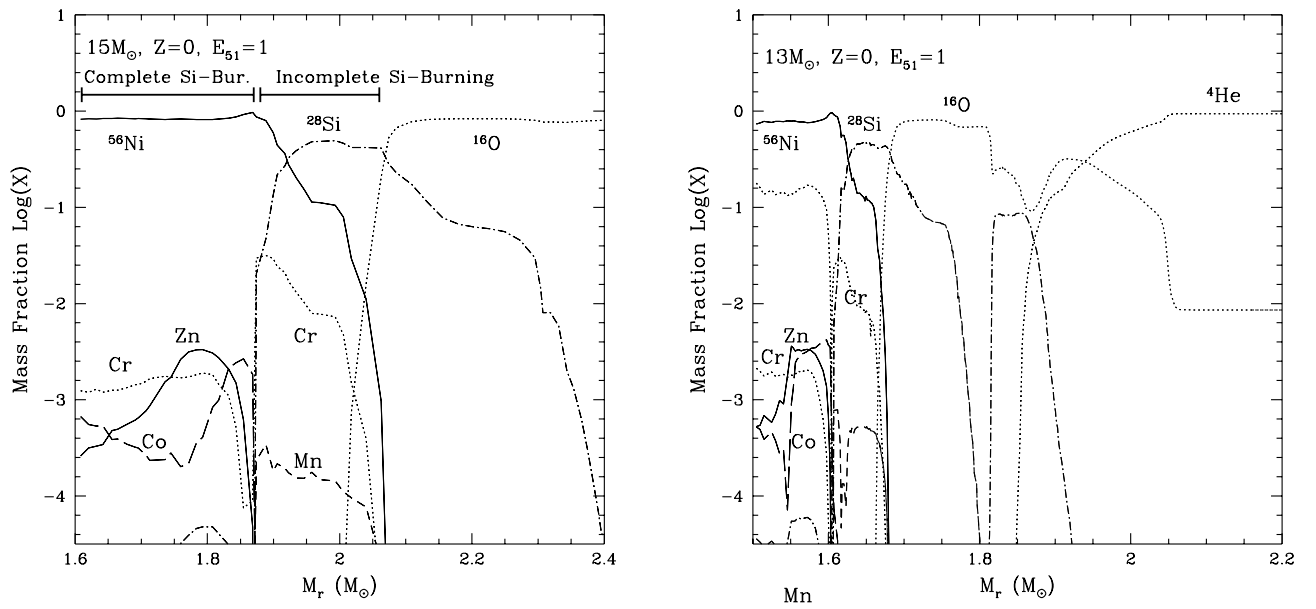


FIG. 3.— Abundance distribution just after supernova explosion. The left and right panels are Pop III models with masses $15M_{\odot}$ and $13M_{\odot}$, respectively. The lines labeled by Cr, Mn, Co and Zn actually indicate unstable ^{52}Fe , ^{55}Co , ^{59}Cu , and ^{64}Ge , respectively, which eventually decay to the labeled elements.

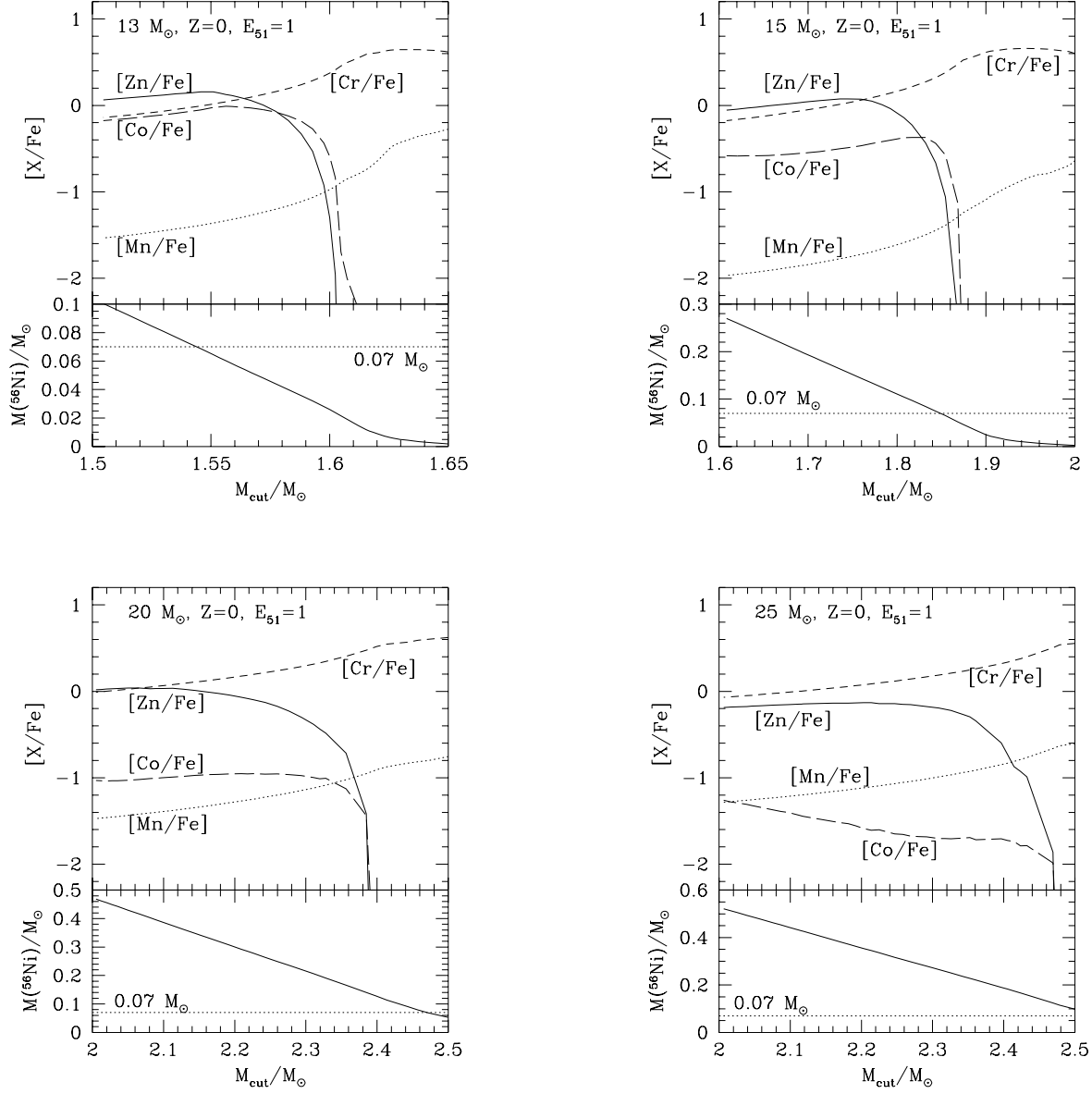


FIG. 4.— Dependence of abundance ratios on the mass coordinate at the mass-cut, M_{cut} , for Pop III SNe II with $E_{51} = 1$.

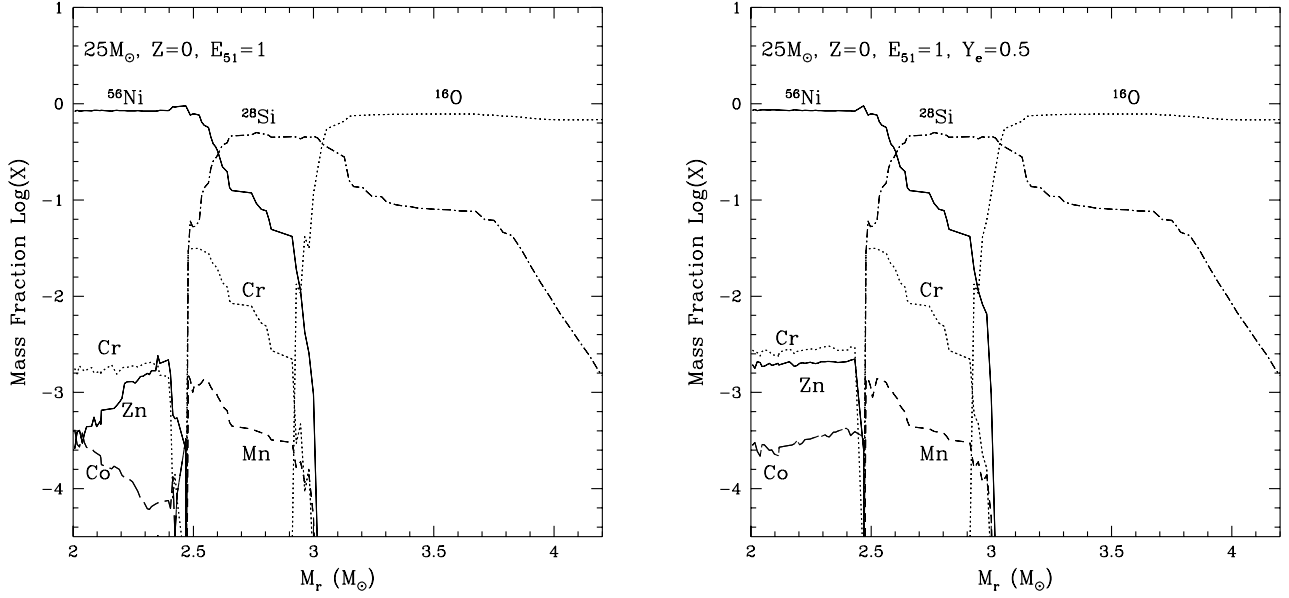


FIG. 5.— Abundance distribution after supernova explosions of Pop III $25M_\odot$ stars with $E_{51} = 1$. The left panel is the original model. In the right panel Y_e is modified to be 0.5 below $M_r = 2.5M_\odot$.

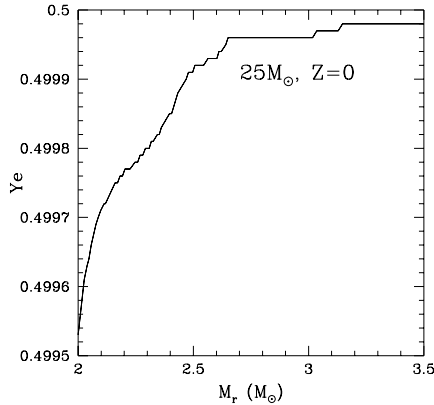


FIG. 6.— The distribution of Y_e in the Pop III $25M_\odot$ model shown in Figure 5.

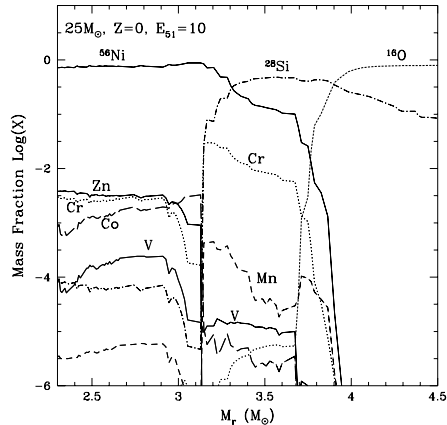


FIG. 7.— Abundance distributions after the supernova explosion of a Pop III $25M_\odot$ star with $E_{\text{exp}} = 10^{52}$ erg. In this figure, distribution of ^{51}Mn which decays into V is also shown.

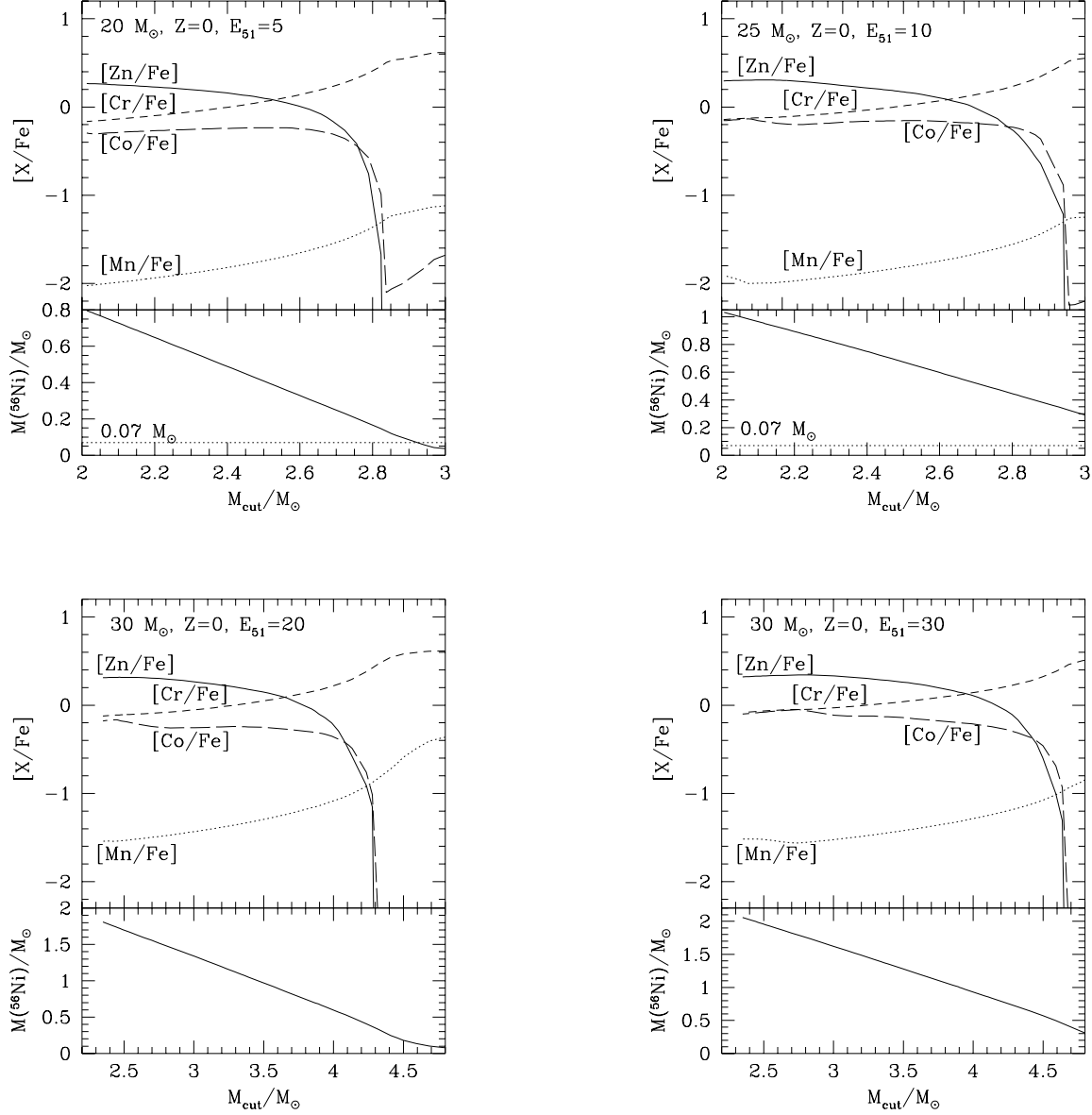


FIG. 8.— Same as Figure 4, but for the energetic SNe II of $M = 20 - 30M_{\odot}$.

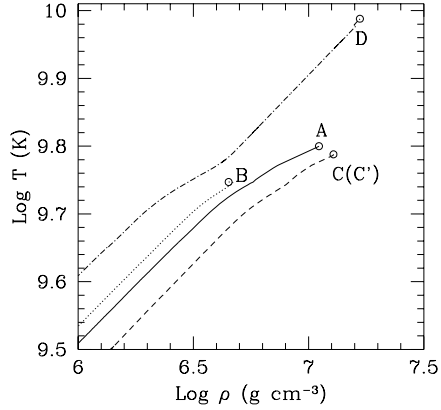


FIG. 9.— Density - temperature tracks during explosive Si-burning for representative cases. Here, the parameters of Cases A, B, C, C' and D are summarized in Table 3.

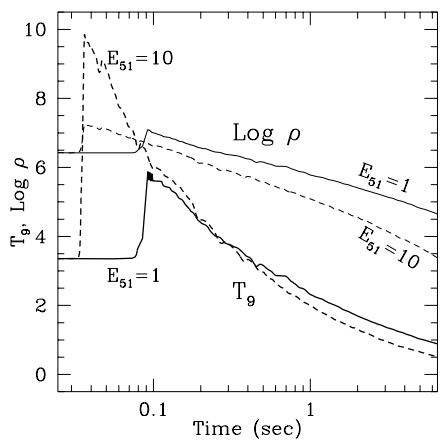


FIG. 10.— Density and Temperature evolution for the cases C, C' ($E_{51}=1$) and D ($E_{51}=10$) in Figure 9. Here $T_9 = T/10^9$ (K), and ρ in $g cm^{-3}$.

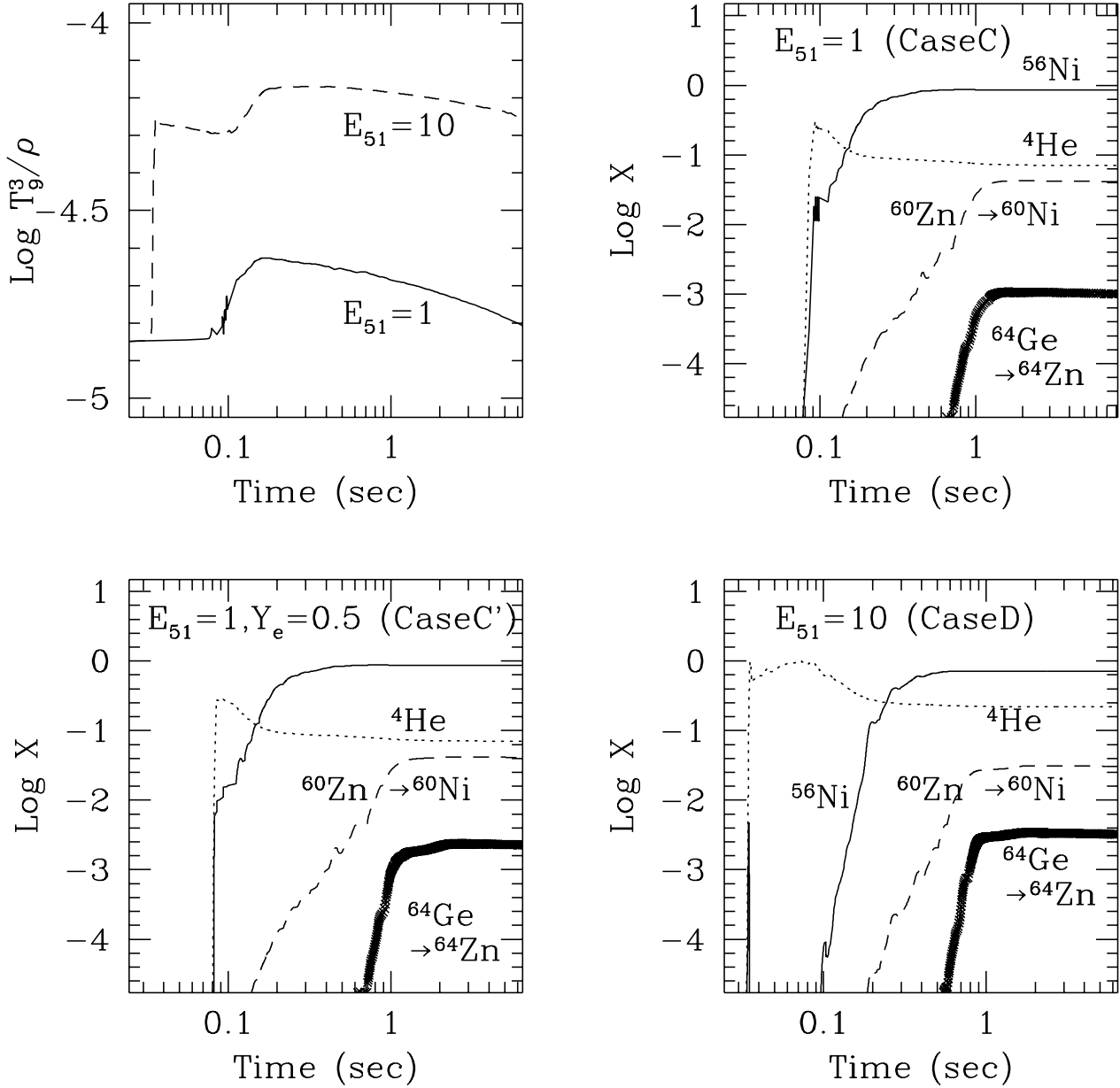


FIG. 11.— Time evolution of T^3/ρ for the cases C, C' ($E_{51}=1$) and D ($E_{51}=10$) in Figure 9 (left top panel), and time evolution of mass fraction ratios of some elements most relevant to Zn synthesis for these cases.

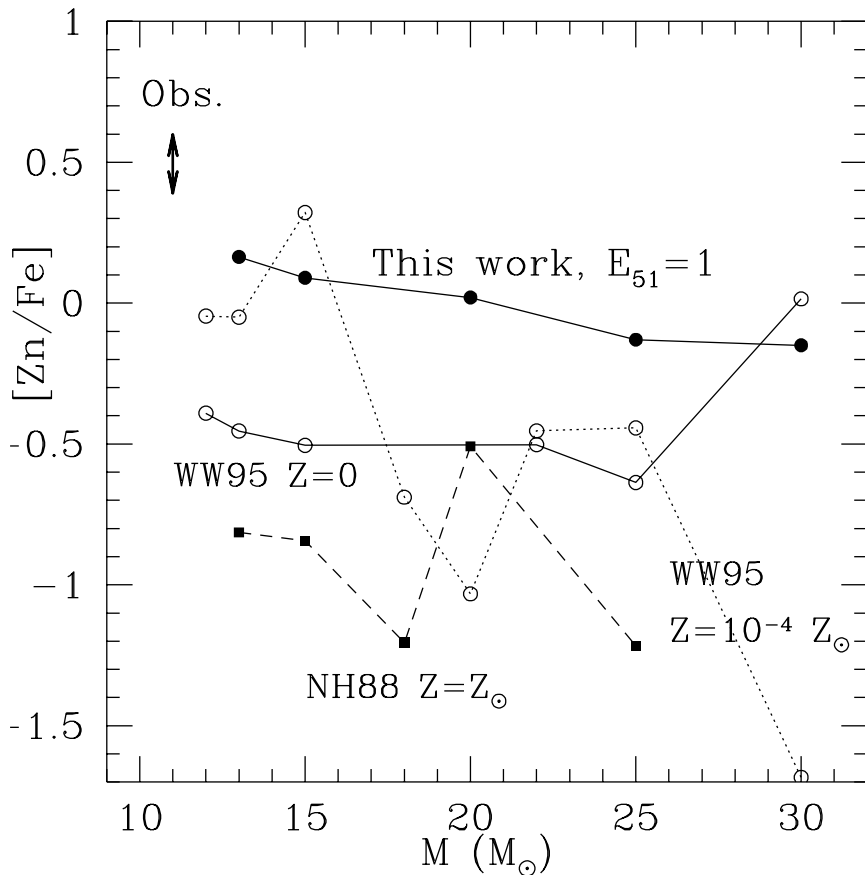


FIG. 12.— [Zn/Fe] ratios of the present and previous works as a function of stellar mass. Here WW95 denotes Woosley & Weaver (1995) and NH88 denotes Nomoto & Hashimoto (1998) models. The observed large [Zn/Fe] ratio in very low-metal stars ($[\text{Fe}/\text{H}] < -2.6$) found in Primas et al. (2000) and Blake et al. (2001) are represented by a thick arrow. The [Zn/Fe] ratios of the present work shown here correspond to the maximum values. If the mass cut is larger the [Zn/Fe] ratios become smaller.

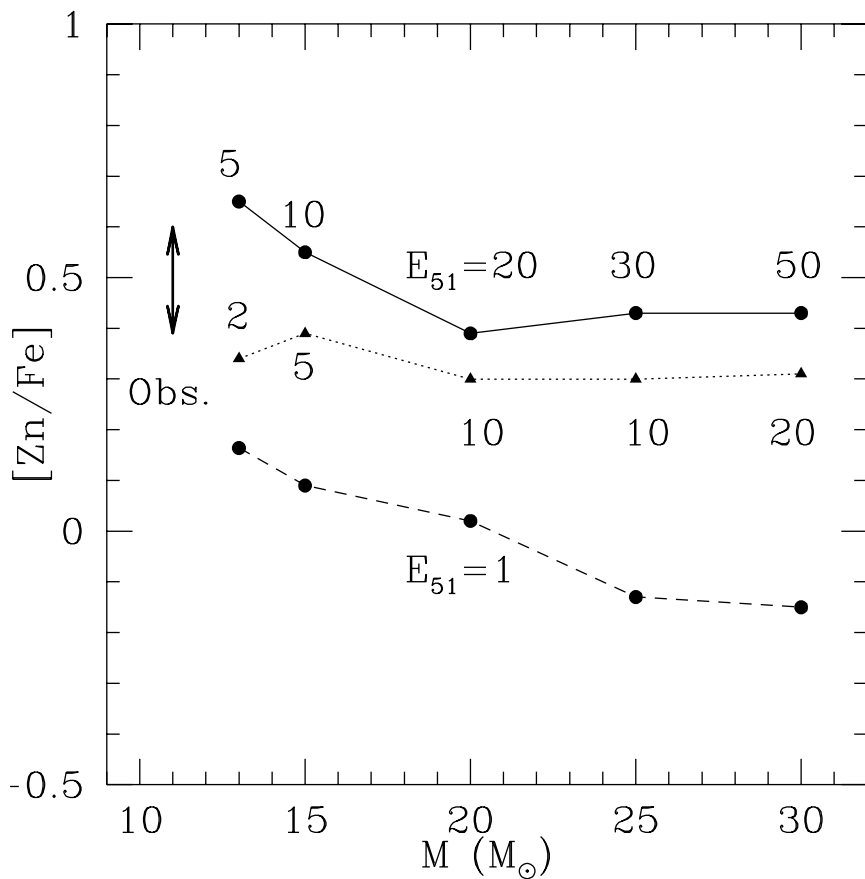


FIG. 13.— The maximum $[Zn/Fe]$ ratios as a function of M and E_{51} . The arrow (obs.) indicates the range of observed high $[Zn/Fe]$ values at $[Fe/H] < -2.6$ (Fig.1).

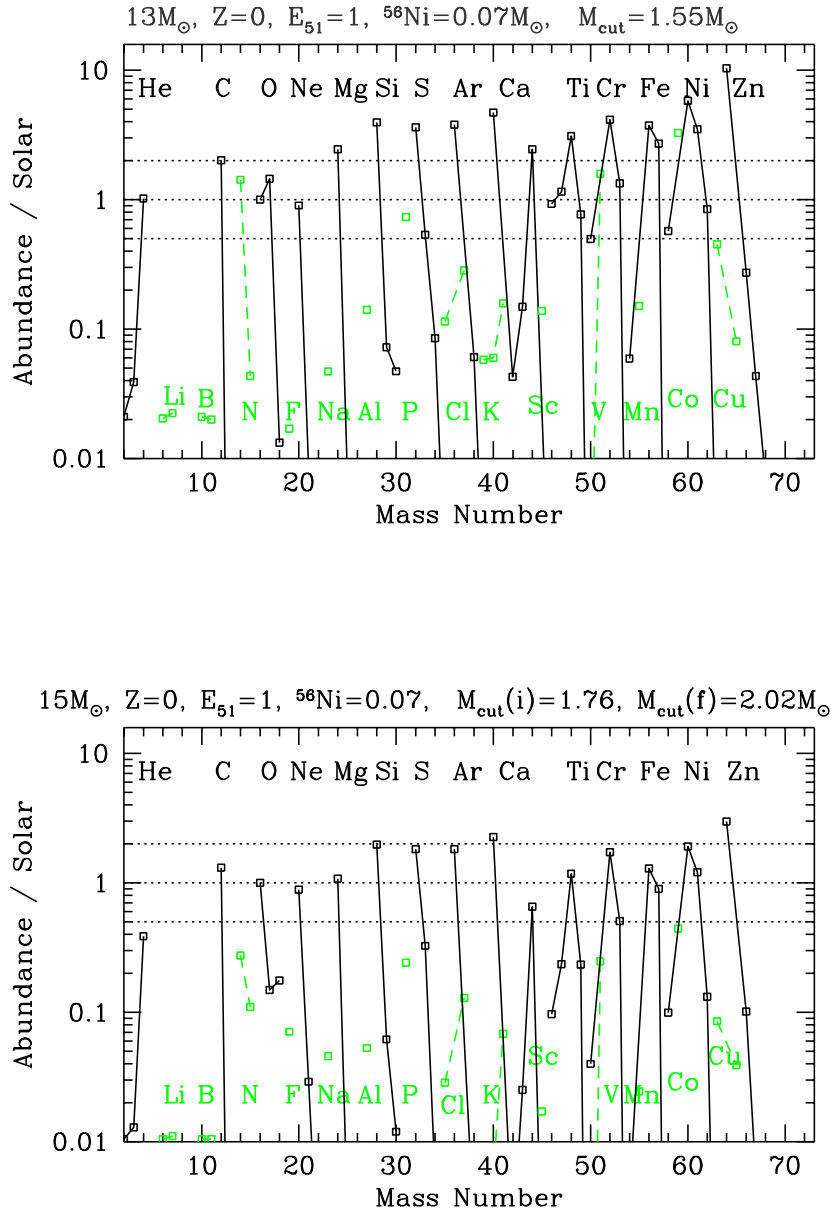


FIG. 14.— Abundance pattern in the ejecta (after radio-active decay) for the $13M_{\odot}$ and $15M_{\odot}$ models normalized by the solar abundances of ^{16}O . Mixing and fall-back is assumed for $15M_{\odot}$ but not for $13M_{\odot}$. The mass-cut is chosen to eject $0.07 M_{\odot}$ ^{56}Ni .

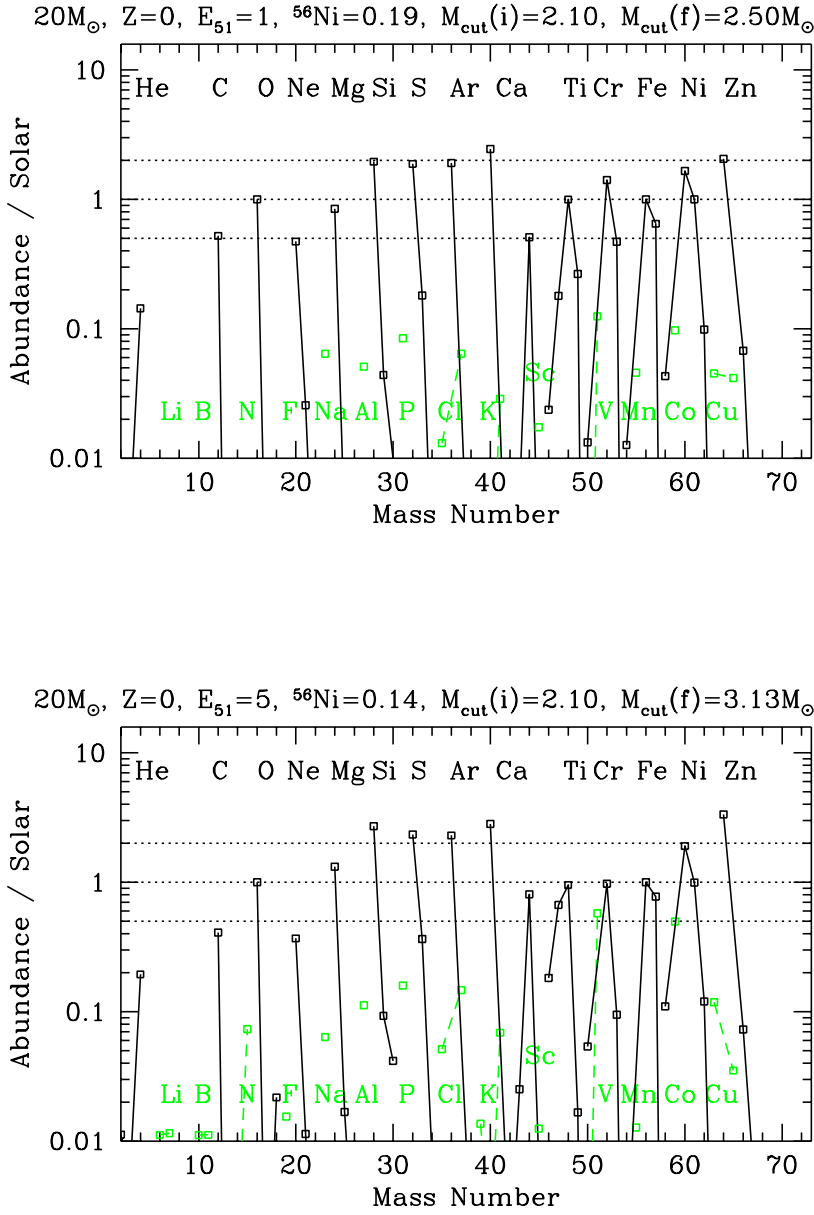


FIG. 15.— Abundance pattern in the ejecta normalized by the solar ¹⁶O abundances for the mixing fall-back 20M_⊙ model with E₅₁ = 1 and 5. The mass-cuts are chosen to give large [Zn/Fe] and [O/Fe]=0.

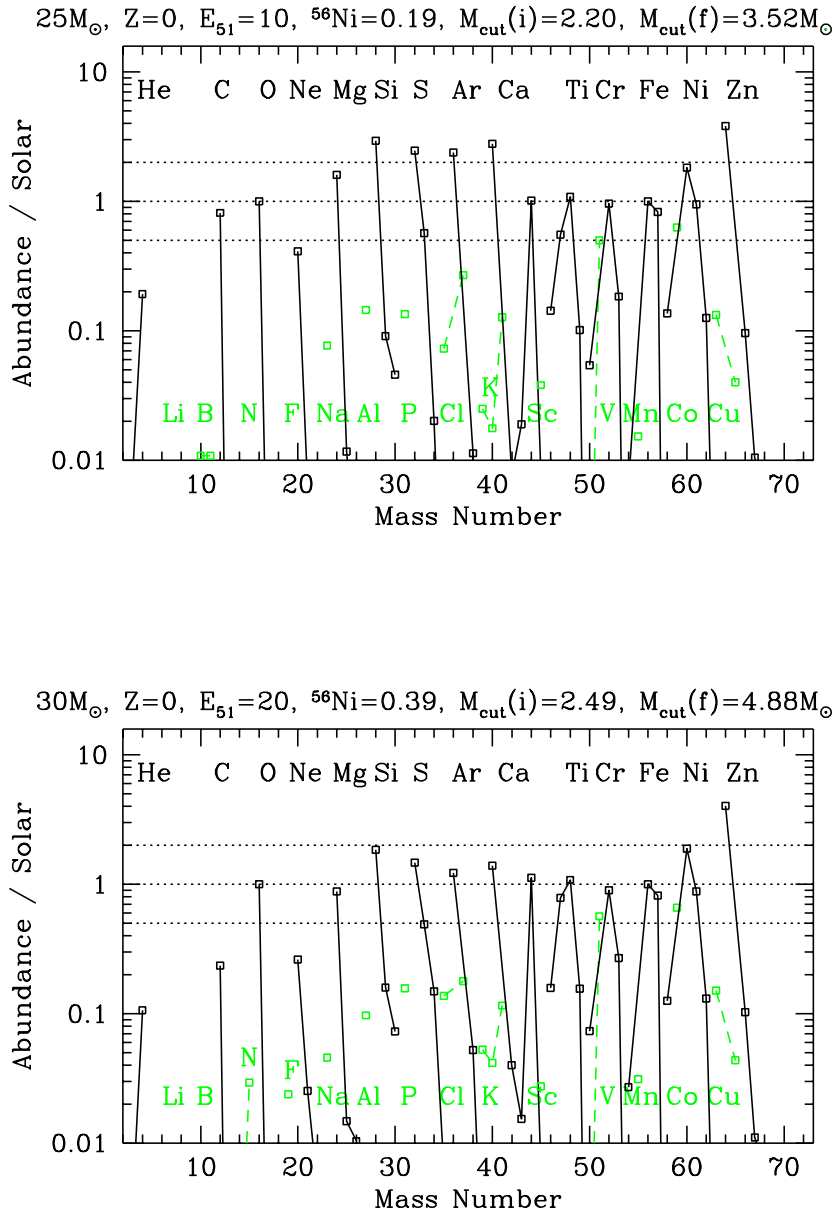


FIG. 16.— Abundance pattern in the ejecta normalized by the solar ^{16}O abundances for the mixing fall-back ($25M_{\odot}$, $E_{51} = 10$) and ($30M_{\odot}$, $E_{51} = 20$) models. The mass-cuts are chosen to give large $[\text{Zn}/\text{Fe}]$ and $[\text{O}/\text{Fe}] = 0$.

Z	Initial Mass (M_{\odot})				
	13	15	20	25	30
0	1.29	1.38	1.52	1.70	1.77
10^{-4}	1.32	—	1.51	—	—
0.02	1.27	1.34	1.52	1.67	—

TABLE 1

“Fe”-core masses in M_{\odot} defined as a region with $Y_e \leq 0.49$ for the progenitor models with $Z = 0, 10^{-4}$ and 0.02.

(M, E_{51})	M_r (incomplete Si-b.)	$\Delta M(^{56}\text{Ni})$
(13, 1)	1.60 – 1.67	0.022
(15, 1)	1.87 – 2.06	0.052
(20, 1)	2.38 – 2.88	0.14
(20, 5)	2.82 – 3.38	0.15
(25, 1)	2.47 – 3.00	0.12
(25, 10)	3.13 – 3.87	0.18
(30, 1)	2.70 – 3.67	0.35
(30, 20)	4.28 – 5.58	0.36
(30, 30)	4.64 – 6.32	0.45

TABLE 2

The mass coordinates in M_{\odot} of the incomplete Si-burning regions for models with several initial masses and explosion energies. The upper and lower bounds of the regions are defined by $X(^{56}\text{Ni}) = 10^{-3}$ and $X(^{28}\text{Si}) = 10^{-4}$, respectively. The ^{56}Ni mass in M_{\odot} in these regions, $\Delta M(^{56}\text{Ni})$, are also shown.

Case	$(M/M_{\odot}, E_{51}, M_r/M_{\odot})$	Y_e	$X(^{56}\text{Ni})$	$X(\text{Zn})$
A	(13, 1, 1.52)	0.4996	7.65E-01	6.04E-04
B	(13, 1, 1.57)	0.4999	7.61E-01	3.46E-03
C	(25, 1, 2.2)	0.4998	8.48E-01	8.89E-04
C'	(25, 1, 2.2)	0.5000	8.55E-01	2.01E-03
D	(25, 10, 2.2)	0.4998	7.12E-01	3.36E-03

TABLE 3

Mass fractions of ^{56}Ni and Zn (decay products of ^{64}Ge) after explosive nucleosynthesis for representative cases shown in Figure 9.

(M, E_{51})	$M_{\text{cut}}(i)$	M_{Si}	$M_{\text{cut}}(f)$	$M(^{56}\text{Ni})$	[O/Fe]	[Zn/Fe]
(13, 1)	1.54	1.67	1.54	0.070	-0.54	0.16
(15, 1)	1.76	2.06	2.02	0.070	-0.08	0.09
(20, 1)	2.10	2.88	2.73 (2.50)	0.070 (0.19)	0.43 (0.0)	0.02
(20, 5)	2.10	3.38	3.27 (3.13)	0.070 (0.14)	0.31 (0.0)	0.24
(25, 1)	2.20	3.00	2.80 (2.40)	0.089 (0.27)	0.50 (0.0)	-0.13
(25, 10)	2.20	3.86	3.74 (3.52)	0.070 (0.19)	0.45 (0.0)	0.30
(25, 30)	2.50	4.52	4.39 (4.27)	0.070 (0.14)	0.28 (0.0)	0.43
(30, 1)	2.26	3.66	3.29 (2.57)	0.20 (0.58)	0.50 (0.0)	-0.18
(30, 20)	2.49	5.58	5.36 (4.87)	0.12 (0.39)	0.50 (0.0)	0.32
(30, 30)	2.83	6.01	5.81 (5.36)	0.11 (0.36)	0.50 (0.0)	0.34
(30, 50)	3.15	6.92	6.74 (6.35)	0.087 (0.28)	0.50 (0.0)	0.43

TABLE 4

Ejected ^{56}Ni mass, [Zn/Fe] and [O/Fe] ratios in the ejecta of mixing fall-back models. In these models, the matter is first uniformly mixed between $M_r = M_{\text{cut}}(i)$ and top of the incomplete Si-burning region $M_r = M_{\text{Si}}$, then the matter below $M_r = M_{\text{cut}}(f)$ is fallen back. For the models with $M \geq 20M_{\odot}$ two choices of $M_{\text{cut}}(f)$ are shown, that gives relatively large [O/Fe] ($\sim 0.3 - 0.5$) and small [O/Fe] (~ 0) ratios. Here $M_{\text{cut}}(f)$ is chosen to eject no less than $0.07M_{\odot}$ of ^{56}Ni .

p	6.666E+00	d	7.754E-06	^3He	2.139E-05	^4He	4.317E+00	^6Li	2.092E-10
^7Li	3.338E-09	^9Be	5.416E-20	^{10}B	3.504E-10	^{11}B	1.501E-09	^{12}C	9.763E-02
^{13}C	1.625E-09	^{14}N	2.519E-02	^{15}N	3.034E-06	^{16}O	1.535E-01	^{17}O	9.014E-05
^{18}O	4.601E-06	^{19}F	1.103E-07	^{20}Ne	2.336E-02	^{21}Ne	5.655E-07	^{22}Ne	7.747E-07
^{23}Na	2.516E-05	^{24}Mg	2.020E-02	^{25}Mg	7.049E-06	^{26}Mg	2.237E-06	^{26}Al	5.961E-07
^{27}Al	1.311E-04	^{28}Si	4.122E-02	^{29}Si	3.958E-05	^{30}Si	1.777E-05	^{31}P	1.575E-05
^{32}S	2.296E-02	^{33}S	2.761E-05	^{34}S	2.536E-05	^{36}S	2.814E-11	^{35}Cl	4.627E-06
^{37}Cl	3.885E-06	^{36}Ar	4.715E-03	^{38}Ar	1.492E-05	^{40}Ar	6.183E-12	^{39}K	3.212E-06
^{40}K	4.259E-10	^{41}K	6.640E-07	^{40}Ca	4.517E-03	^{42}Ca	2.878E-07	^{43}Ca	2.140E-07
^{44}Ca	5.556E-05	^{46}Ca	9.666E-12	^{48}Ca	2.223E-12	^{45}Sc	8.608E-08	^{46}Ti	3.314E-06
^{47}Ti	3.842E-06	^{48}Ti	1.070E-04	^{49}Ti	2.014E-06	^{50}Ti	1.842E-11	^{50}V	1.065E-11
^{51}V	9.538E-06	^{50}Cr	5.917E-06	^{52}Cr	9.887E-04	^{53}Cr	3.686E-05	^{54}Cr	6.145E-11
^{55}Mn	3.211E-05	^{54}Fe	6.735E-05	^{56}Fe	7.000E-02	^{57}Fe	1.242E-03	^{58}Fe	6.629E-11
^{59}Co	1.759E-04	^{58}Ni	4.522E-04	^{60}Ni	1.815E-03	^{61}Ni	4.806E-05	^{62}Ni	3.758E-05
^{64}Ni	1.499E-11	^{63}Cu	4.167E-06	^{65}Cu	3.403E-07	^{64}Zn	1.643E-04	^{66}Zn	2.560E-06
^{67}Zn	6.092E-08	^{68}Zn	4.653E-08	^{70}Zn	1.434E-11	^{69}Ga	5.899E-09	^{71}Ga	4.674E-11
^{70}Ge	1.281E-08	^{72}Ge	3.285E-11	^{73}Ge	4.584E-11	^{74}Ge	1.863E-11		

TABLE 5

Yields in the ejecta in M_{\odot} after radio active decay (except ^{26}Al) for the $13M_{\odot}$ $E_{51} = 1$ model shown in Table 4. ($M_{\text{cut}}(i)$, M_{Si} , $M_{\text{cut}}(f)$)=(1.54, 1.67, 1.54), [O/Fe]=-0.54 and [Zn/Fe]=0.16.

p	7.581E+00	d	1.117E-05	³ He	2.052E-05	⁴ He	4.727E+00	⁶ Li	3.100E-10
⁷ Li	4.748E-09	⁹ Be	2.242E-21	¹⁰ B	5.057E-10	¹¹ B	2.277E-09	¹² C	1.839E-01
¹³ C	8.899E-09	¹⁴ N	1.404E-02	¹⁵ N	2.219E-05	¹⁶ O	4.434E-01	¹⁷ O	2.676E-05
¹⁸ O	1.767E-04	¹⁹ F	1.324E-06	²⁰ Ne	6.639E-02	²¹ Ne	5.543E-06	²² Ne	4.458E-06
²³ Na	7.051E-05	²⁴ Mg	2.570E-02	²⁵ Mg	7.822E-06	²⁶ Mg	4.186E-06	²⁶ Al	2.424E-07
²⁷ Al	1.419E-04	²⁸ Si	5.974E-02	²⁹ Si	9.778E-05	³⁰ Si	1.299E-05	³¹ P	1.102E-05
³² S	3.330E-02	³³ S	4.855E-05	³⁴ S	4.504E-06	³⁶ S	7.750E-12	³⁵ Cl	3.337E-06
³⁷ Cl	5.086E-06	³⁶ Ar	6.509E-03	³⁸ Ar	1.460E-06	⁴⁰ Ar	1.588E-13	³⁹ K	1.316E-06
⁴⁰ K	1.093E-10	⁴¹ K	8.288E-07	⁴⁰ Ca	6.247E-03	⁴² Ca	3.242E-08	⁴³ Ca	1.040E-07
⁴⁴ Ca	4.292E-05	⁴⁶ Ca	1.043E-13	⁴⁸ Ca	9.289E-14	⁴⁵ Sc	3.088E-08	⁴⁶ Ti	9.959E-07
⁴⁷ Ti	2.265E-06	⁴⁸ Ti	1.166E-04	⁴⁹ Ti	1.762E-06	⁵⁰ Ti	2.016E-13	⁵⁰ V	2.425E-13
⁵¹ V	4.311E-06	⁵⁰ Cr	1.368E-06	⁵² Cr	1.184E-03	⁵³ Cr	4.033E-05	⁵⁴ Cr	2.895E-12
⁵⁵ Mn	1.505E-05	⁵⁴ Fe	1.292E-05	⁵⁶ Fe	7.000E-02	⁵⁷ Fe	1.188E-03	⁵⁸ Fe	1.390E-11
⁵⁹ Co	6.883E-05	⁵⁸ Ni	2.275E-04	⁶⁰ Ni	1.729E-03	⁶¹ Ni	4.813E-05	⁶² Ni	1.689E-05
⁶⁴ Ni	3.083E-13	⁶³ Cu	2.269E-06	⁶⁵ Cu	4.774E-07	⁶⁴ Zn	1.368E-04	⁶⁶ Zn	2.761E-06
⁶⁷ Zn	2.314E-08	⁶⁸ Zn	3.672E-08	⁷⁰ Zn	2.685E-13	⁶⁹ Ga	4.957E-09	⁷¹ Ga	8.216E-13
⁷⁰ Ge	1.152E-08	⁷² Ge	1.664E-12	⁷³ Ge	9.740E-13	⁷⁴ Ge	1.081E-12		

TABLE 6

Yields in the ejecta in M_{\odot} after radio active decay (except ^{26}Al) for the $15M_{\odot}$ $E_{51} = 1$ model shown in Table 4. ($M_{\text{cut}}(i)$, M_{Si} , $M_{\text{cut}}(f)) = (1.76, 2.06, 2.02)$, $[\text{O}/\text{Fe}] = -0.08$ and $[\text{Zn}/\text{Fe}] = 0.09$.

p	9.396E+00	d	2.768E-05	³ He	2.556E-05	⁴ He	6.258E+00	⁶ Li	7.648E-10
⁷ Li	1.154E-08	⁹ Be	4.661E-19	¹⁰ B	1.252E-09	¹¹ B	5.613E-09	¹² C	2.569E-01
¹³ C	4.559E-08	¹⁴ N	2.688E-04	¹⁵ N	1.769E-06	¹⁶ O	1.550E+00	¹⁷ O	2.385E-07
¹⁸ O	4.878E-06	¹⁹ F	3.298E-07	²⁰ Ne	1.240E-01	²¹ Ne	1.721E-05	²² Ne	1.177E-05
²³ Na	3.468E-04	²⁴ Mg	7.069E-02	²⁵ Mg	3.046E-05	²⁶ Mg	1.878E-05	²⁶ Al	9.127E-07
²⁷ Al	4.785E-04	²⁸ Si	9.815E-02	²⁹ Si	2.423E-04	³⁰ Si	3.682E-05	³¹ P	2.750E-05
³² S	4.118E-02	³³ S	8.979E-05	³⁴ S	2.003E-06	³⁶ S	3.230E-12	³⁵ Cl	3.677E-06
³⁷ Cl	7.208E-06	³⁶ Ar	6.904E-03	³⁸ Ar	4.062E-07	⁴⁰ Ar	7.280E-13	³⁹ K	9.696E-07
⁴⁰ K	3.596E-11	⁴¹ K	7.139E-07	⁴⁰ Ca	6.124E-03	⁴² Ca	9.075E-09	⁴³ Ca	2.692E-08
⁴⁴ Ca	4.355E-05	⁴⁶ Ca	1.022E-12	⁴⁸ Ca	2.924E-13	⁴⁵ Sc	3.251E-08	⁴⁶ Ti	3.250E-07
⁴⁷ Ti	2.290E-06	⁴⁸ Ti	1.205E-04	⁴⁹ Ti	2.106E-06	⁵⁰ Ti	3.776E-13	⁵⁰ V	3.424E-13
⁵¹ V	2.800E-06	⁵⁰ Cr	5.588E-07	⁵² Cr	1.190E-03	⁵³ Cr	4.325E-05	⁵⁴ Cr	2.661E-12
⁵⁵ Mn	3.223E-05	⁵⁴ Fe	4.456E-05	⁵⁶ Fe	7.000E-02	⁵⁷ Fe	1.120E-03	⁵⁸ Fe	5.539E-12
⁵⁹ Co	2.009E-05	⁵⁸ Ni	1.154E-04	⁶⁰ Ni	1.995E-03	⁶¹ Ni	5.286E-05	⁶² Ni	1.684E-05
⁶⁴ Ni	1.030E-12	⁶³ Cu	1.591E-06	⁶⁵ Cu	6.779E-07	⁶⁴ Zn	1.249E-04	⁶⁶ Zn	2.438E-06
⁶⁷ Zn	9.175E-09	⁶⁸ Zn	9.031E-08	⁷⁰ Zn	7.743E-13	⁶⁹ Ga	9.441E-09	⁷¹ Ga	3.297E-12
⁷⁰ Ge	1.064E-08	⁷² Ge	6.328E-12	⁷³ Ge	3.331E-12	⁷⁴ Ge	2.699E-12		

TABLE 7

Yields in the ejecta in M_{\odot} after radio active decay (except ^{26}Al) for the $20M_{\odot}$ $E_{51} = 1$ model shown in Table 4. ($M_{\text{cut}}(i)$, M_{Si} , $M_{\text{cut}}(f)) = (2.10, 2.88, 2.73)$, $[\text{O}/\text{Fe}] = 0.43$ and $[\text{Zn}/\text{Fe}] = 0.02$.

p	1.081E+01	d	6.294E-17	³ He	3.929E-05	⁴ He	7.929E+00	⁶ Li	7.899E-22
⁷ Li	3.344E-10	⁹ Be	1.223E-19	¹⁰ B	6.319E-10	¹¹ B	2.534E-09	¹² C	6.138E-01
¹³ C	4.218E-08	¹⁴ N	3.583E-04	¹⁵ N	8.050E-08	¹⁶ O	2.177E+00	¹⁷ O	1.707E-07
¹⁸ O	1.964E-06	¹⁹ F	4.055E-10	²⁰ Ne	2.034E-01	²¹ Ne	2.129E-05	²² Ne	1.302E-05
²³ Na	9.229E-04	²⁴ Mg	1.172E-01	²⁵ Mg	8.523E-05	²⁶ Mg	6.545E-05	²⁶ Al	2.251E-06
²⁷ Al	1.115E-03	²⁸ Si	1.631E-01	²⁹ Si	4.945E-04	³⁰ Si	9.131E-05	³¹ P	6.875E-05
³² S	6.761E-02	³³ S	1.790E-04	³⁴ S	4.339E-05	³⁶ S	8.673E-11	³⁵ Cl	1.369E-05
³⁷ Cl	1.429E-05	³⁶ Ar	1.093E-02	³⁸ Ar	1.826E-05	⁴⁰ Ar	1.641E-12	³⁹ K	5.902E-06
⁴⁰ K	6.253E-10	⁴¹ K	1.605E-06	⁴⁰ Ca	9.370E-03	⁴² Ca	3.438E-07	⁴³ Ca	8.692E-08
⁴⁴ Ca	7.142E-05	⁴⁶ Ca	4.504E-13	⁴⁸ Ca	4.037E-13	⁴⁵ Sc	5.783E-08	⁴⁶ Ti	1.360E-07
⁴⁷ Ti	3.508E-07	⁴⁸ Ti	1.714E-04	⁴⁹ Ti	3.020E-06	⁵⁰ Ti	3.396E-13	⁵⁰ V	1.741E-12
⁵¹ V	1.412E-06	⁵⁰ Cr	1.614E-06	⁵² Cr	1.558E-03	⁵³ Cr	6.067E-05	⁵⁴ Cr	4.511E-11
⁵⁵ Mn	7.805E-05	⁵⁴ Fe	2.121E-04	⁵⁶ Fe	8.941E-02	⁵⁷ Fe	1.640E-03	⁵⁸ Fe	7.253E-11
⁵⁹ Co	6.672E-06	⁵⁸ Ni	1.092E-04	⁶⁰ Ni	2.385E-03	⁶¹ Ni	8.696E-05	⁶² Ni	7.567E-05
⁶⁴ Ni	4.090E-12	⁶³ Cu	9.255E-07	⁶⁵ Cu	1.211E-06	⁶⁴ Zn	1.094E-04	⁶⁶ Zn	4.751E-06
⁶⁷ Zn	3.077E-09	⁶⁸ Zn	1.742E-08	⁷⁰ Zn	1.304E-12	⁶⁹ Ga	3.980E-09	⁷¹ Ga	4.263E-12
⁷⁰ Ge	1.597E-08	⁷² Ge	1.003E-11	⁷³ Ge	4.500E-12	⁷⁴ Ge	1.840E-12		

TABLE 8

Yields in the ejecta in M_{\odot} after radio active decay (except ^{26}Al) for the $25M_{\odot} E_{51} = 1$ model shown in Table 4. ($M_{\text{cut}}(i)$, M_{Si} , $M_{\text{cut}}(f) = (2.20, 3.00, 2.80)$, $[\text{O}/\text{Fe}] = 0.50$ and $[\text{Zn}/\text{Fe}] = -0.13$.

p	1.083E+01	d	4.890E-16	³ He	3.931E-05	⁴ He	7.899E+00	⁶ Li	2.211E-18
⁷ Li	3.320E-10	⁹ Be	1.189E-21	¹⁰ B	6.579E-10	¹¹ B	2.955E-09	¹² C	3.987E-01
¹³ C	4.442E-08	¹⁴ N	7.193E-04	¹⁵ N	3.131E-06	¹⁶ O	1.534E+00	¹⁷ O	1.598E-07
¹⁸ O	2.115E-05	¹⁹ F	5.244E-07	²⁰ Ne	1.075E-01	²¹ Ne	4.190E-06	²² Ne	6.660E-06
²³ Na	4.155E-04	²⁴ Mg	1.329E-01	²⁵ Mg	1.276E-04	²⁶ Mg	2.536E-05	²⁶ Al	1.960E-06
²⁷ Al	1.354E-03	²⁸ Si	1.981E-01	²⁹ Si	5.011E-04	³⁰ Si	1.711E-04	³¹ P	9.133E-05
³² S	7.179E-02	³³ S	2.893E-04	³⁴ S	5.153E-05	³⁶ S	6.776E-11	³⁵ Cl	2.316E-05
³⁷ Cl	3.447E-05	³⁶ Ar	1.028E-02	³⁸ Ar	2.580E-05	⁴⁰ Ar	1.052E-11	³⁹ K	1.057E-05
⁴⁰ K	1.268E-09	⁴¹ K	4.468E-06	⁴⁰ Ca	6.155E-03	⁴² Ca	5.070E-07	⁴³ Ca	1.042E-07
⁴⁴ Ca	8.673E-05	⁴⁶ Ca	2.959E-11	⁴⁸ Ca	1.654E-11	⁴⁵ Sc	9.992E-08	⁴⁶ Ti	2.076E-06
⁴⁷ Ti	7.047E-06	⁴⁸ Ti	1.334E-04	⁴⁹ Ti	4.576E-07	⁵⁰ Ti	1.791E-11	⁵⁰ V	2.659E-11
⁵¹ V	1.148E-05	⁵⁰ Cr	2.797E-06	⁵² Cr	8.058E-04	⁵³ Cr	1.356E-05	⁵⁴ Cr	1.085E-10
⁵⁵ Mn	8.665E-06	⁵⁴ Fe	2.672E-05	⁵⁶ Fe	7.000E-02	⁵⁷ Fe	1.422E-03	⁵⁸ Fe	1.808E-10
⁵⁹ Co	1.297E-04	⁵⁸ Ni	3.767E-04	⁶⁰ Ni	2.190E-03	⁶¹ Ni	5.001E-05	⁶² Ni	2.136E-05
⁶⁴ Ni	4.488E-11	⁶³ Cu	4.671E-06	⁶⁵ Cu	6.493E-07	⁶⁴ Zn	2.319E-04	⁶⁶ Zn	3.467E-06
⁶⁷ Zn	5.623E-08	⁶⁸ Zn	1.101E-07	⁷⁰ Zn	2.816E-11	⁶⁹ Ga	1.237E-08	⁷¹ Ga	9.127E-11
⁷⁰ Ge	1.412E-08	⁷² Ge	9.611E-11	⁷³ Ge	1.201E-10	⁷⁴ Ge	5.454E-11		

TABLE 9

Yields in the ejecta in M_{\odot} after radio active decay (except ^{26}Al) for the $25M_{\odot} E_{51} = 10$ model shown in Table 4. ($M_{\text{cut}}(i)$, M_{Si} , $M_{\text{cut}}(f) = (2.20, 3.86, 3.74)$, $[\text{O}/\text{Fe}] = 0.45$ and $[\text{Zn}/\text{Fe}] = 0.30$.

p	1.083E+01	d	1.268E-16	³ He	3.931E-05	⁴ He	7.783E+00	⁶ Li	2.978E-19
⁷ Li	3.319E-10	⁹ Be	3.498E-22	¹⁰ B	6.588E-10	¹¹ B	2.963E-09	¹² C	1.659E-01
¹³ C	7.908E-09	¹⁴ N	2.099E-03	¹⁵ N	1.527E-04	¹⁶ O	1.030E+00	¹⁷ O	5.606E-08
¹⁸ O	8.921E-05	¹⁹ F	2.381E-06	²⁰ Ne	5.912E-02	²¹ Ne	1.319E-06	²² Ne	2.799E-06
²³ Na	2.001E-04	²⁴ Mg	1.226E-01	²⁵ Mg	3.482E-05	²⁶ Mg	4.364E-06	²⁶ Al	5.487E-05
²⁷ Al	1.284E-03	²⁸ Si	3.412E-01	²⁹ Si	1.363E-03	³⁰ Si	3.504E-04	³¹ P	3.646E-04
³² S	1.571E-01	³³ S	3.029E-04	³⁴ S	5.753E-05	³⁶ S	1.978E-11	³⁵ Cl	5.579E-05
³⁷ Cl	6.283E-05	³⁶ Ar	2.352E-02	³⁸ Ar	2.906E-05	⁴⁰ Ar	8.835E-12	³⁹ K	1.701E-05
⁴⁰ K	1.299E-09	⁴¹ K	1.001E-05	⁴⁰ Ca	1.500E-02	⁴² Ca	8.096E-07	⁴³ Ca	2.856E-07
⁴⁴ Ca	1.286E-04	⁴⁶ Ca	9.054E-11	⁴⁸ Ca	1.528E-11	⁴⁵ Sc	5.722E-07	⁴⁶ Ti	3.519E-06
⁴⁷ Ti	1.033E-05	⁴⁸ Ti	1.758E-04	⁴⁹ Ti	2.926E-06	⁵⁰ Ti	1.574E-10	⁵⁰ V	9.977E-11
⁵¹ V	2.236E-05	⁵⁰ Cr	7.384E-06	⁵² Cr	8.749E-04	⁵³ Cr	4.865E-06	⁵⁴ Cr	3.043E-10
⁵⁵ Mn	1.670E-05	⁵⁴ Fe	2.406E-05	⁵⁶ Fe	7.000E-02	⁵⁷ Fe	1.241E-03	⁵⁸ Fe	5.608E-10
⁵⁹ Co	3.471E-04	⁵⁸ Ni	8.285E-04	⁶⁰ Ni	2.258E-03	⁶¹ Ni	3.926E-05	⁶² Ni	2.805E-05
⁶⁴ Ni	1.465E-10	⁶³ Cu	9.108E-06	⁶⁵ Cu	6.024E-07	⁶⁴ Zn	3.128E-04	⁶⁶ Zn	4.406E-06
⁶⁷ Zn	2.284E-07	⁶⁸ Zn	1.078E-07	⁷⁰ Zn	8.656E-11	⁶⁹ Ga	1.440E-08	⁷¹ Ga	8.630E-10
⁷⁰ Ge	1.696E-08	⁷² Ge	8.892E-10	⁷³ Ge	6.904E-10	⁷⁴ Ge	3.390E-10		

TABLE 10

Yields in the ejecta in M_{\odot} after radio active decay (except ²⁶Al) for the $25M_{\odot}$ $E_{51} = 30$ model shown in Table 4. ($M_{\text{cut}}(i)$, M_{Si} , $M_{\text{cut}}(f) = (2.50, 4.52, 4.39)$, [O/Fe]=0.28 and [Zn/Fe]=0.43.

p	1.167E+01	d	2.042E-16	³ He	2.106E-05	⁴ He	8.776E+00	⁶ Li	6.170E-19
⁷ Li	2.938E-10	⁹ Be	6.545E-18	¹⁰ B	5.577E-15	¹¹ B	3.274E-15	¹² C	3.561E-01
¹³ C	1.733E-08	¹⁴ N	1.944E-04	¹⁵ N	1.412E-05	¹⁶ O	4.792E+00	¹⁷ O	7.218E-07
¹⁸ O	4.632E-05	¹⁹ F	1.416E-05	²⁰ Ne	2.720E-01	²¹ Ne	4.170E-05	²² Ne	5.711E-04
²³ Na	3.664E-04	²⁴ Mg	2.379E-01	²⁵ Mg	3.205E-04	²⁶ Mg	1.495E-04	²⁶ Al	2.903E-06
²⁷ Al	5.031E-03	²⁸ Si	2.450E-01	²⁹ Si	1.304E-03	³⁰ Si	9.735E-04	³¹ P	3.842E-04
³² S	1.011E-01	³³ S	2.925E-04	³⁴ S	5.197E-04	³⁶ S	1.018E-08	³⁵ Cl	5.177E-05
³⁷ Cl	1.380E-05	³⁶ Ar	1.711E-02	³⁸ Ar	7.218E-05	⁴⁰ Ar	7.808E-11	³⁹ K	9.494E-06
⁴⁰ K	2.788E-09	⁴¹ K	1.520E-06	⁴⁰ Ca	1.634E-02	⁴² Ca	1.014E-06	⁴³ Ca	6.962E-08
⁴⁴ Ca	1.488E-04	⁴⁶ Ca	7.124E-12	⁴⁸ Ca	1.401E-14	⁴⁵ Sc	8.049E-08	⁴⁶ Ti	2.160E-07
⁴⁷ Ti	4.430E-07	⁴⁸ Ti	3.153E-04	⁴⁹ Ti	5.405E-06	⁵⁰ Ti	9.707E-13	⁵⁰ V	1.146E-11
⁵¹ V	3.209E-06	⁵⁰ Cr	4.571E-06	⁵² Cr	2.804E-03	⁵³ Cr	1.173E-04	⁵⁴ Cr	1.326E-10
⁵⁵ Mn	2.122E-04	⁵⁴ Fe	7.244E-04	⁵⁶ Fe	1.968E-01	⁵⁷ Fe	3.241E-03	⁵⁸ Fe	1.246E-10
⁵⁹ Co	9.233E-06	⁵⁸ Ni	2.733E-04	⁶⁰ Ni	5.399E-03	⁶¹ Ni	2.044E-04	⁶² Ni	1.344E-04
⁶⁴ Ni	3.041E-13	⁶³ Cu	8.295E-07	⁶⁵ Cu	3.492E-06	⁶⁴ Zn	2.159E-04	⁶⁶ Zn	9.159E-06
⁶⁷ Zn	3.475E-09	⁶⁸ Zn	6.713E-08	⁷⁰ Zn	2.637E-13	⁶⁹ Ga	1.018E-08	⁷¹ Ga	7.251E-13
⁷⁰ Ge	2.994E-08	⁷² Ge	1.351E-12	⁷³ Ge	1.038E-12	⁷⁴ Ge	5.457E-13		

TABLE 11

Yields in the ejecta in M_{\odot} after radio active decay (except ²⁶Al) for the $30M_{\odot}$ $E_{51} = 1$ model shown in Table 4. ($M_{\text{cut}}(i)$, M_{Si} , $M_{\text{cut}}(f) = (2.26, 3.66, 3.29)$, [O/Fe]=0.50 and [Zn/Fe]=-0.18.

p	2.148E+02	d	1.664E-15	³ He	1.821E-03	⁴ He	7.543E+01	⁶ Li	1.752E-17
⁷ Li	2.966E-10	⁹ Be	2.780E-21	¹⁰ B	9.314E-15	¹¹ B	1.612E-12	¹² C	1.704E-01
¹³ C	3.273E-08	¹⁴ N	9.203E-05	¹⁵ N	4.360E-05	¹⁶ O	2.761E+00	¹⁷ O	1.554E-07
¹⁸ O	9.132E-05	¹⁹ F	1.098E-06	²⁰ Ne	1.011E-01	²¹ Ne	2.124E-05	²² Ne	1.144E-04
²³ Na	4.131E-04	²⁴ Mg	1.303E-01	²⁵ Mg	2.990E-04	²⁶ Mg	2.649E-04	²⁶ Al	1.703E-05
²⁷ Al	1.134E-03	²⁸ Si	3.708E-01	²⁹ Si	1.170E-03	³⁰ Si	3.732E-04	³¹ P	3.798E-04
³² S	2.081E-01	³³ S	4.947E-04	³⁴ S	7.353E-04	³⁶ S	3.626E-09	³⁵ Cl	2.263E-04
³⁷ Cl	5.457E-05	³⁶ Ar	3.456E-02	³⁸ Ar	2.861E-04	⁴⁰ Ar	9.876E-11	³⁹ K	4.137E-05
⁴⁰ K	6.983E-09	⁴¹ K	8.493E-06	⁴⁰ Ca	2.449E-02	⁴² Ca	5.354E-06	⁴³ Ca	1.699E-07
⁴⁴ Ca	1.745E-04	⁴⁶ Ca	3.572E-11	⁴⁸ Ca	7.367E-12	⁴⁵ Sc	4.161E-07	⁴⁶ Ti	4.628E-06
⁴⁷ Ti	1.373E-05	⁴⁸ Ti	2.510E-04	⁴⁹ Ti	3.173E-06	⁵⁰ Ti	7.185E-11	⁵⁰ V	1.023E-10
⁵¹ V	2.285E-05	⁵⁰ Cr	7.364E-06	⁵² Cr	1.489E-03	⁵³ Cr	5.253E-05	⁵⁴ Cr	4.736E-10
⁵⁵ Mn	6.651E-05	⁵⁴ Fe	6.336E-04	⁵⁶ Fe	1.127E-01	⁵⁷ Fe	2.227E-03	⁵⁸ Fe	3.411E-10
⁵⁹ Co	2.753E-04	⁵⁸ Ni	1.038E-03	⁶⁰ Ni	3.353E-03	⁶¹ Ni	6.804E-05	⁶² Ni	3.645E-05
⁶⁴ Ni	7.030E-11	⁶³ Cu	9.326E-06	⁶⁵ Cu	1.050E-06	⁶⁴ Zn	4.082E-04	⁶⁶ Zn	6.260E-06
⁶⁷ Zn	1.546E-07	⁶⁸ Zn	1.949E-07	⁷⁰ Zn	7.280E-11	⁶⁹ Ga	2.222E-08	⁷¹ Ga	2.880E-10
⁷⁰ Ge	2.167E-08	⁷² Ge	1.853E-10	⁷³ Ge	3.036E-10	⁷⁴ Ge	1.292E-10		

TABLE 12

Yields in the ejecta in M_{\odot} after radio active decay (except ^{26}Al) for the $30M_{\odot} E_{51} = 30$ model shown in Table 4. ($M_{\text{cut}}(i)$, M_{Si} , $M_{\text{cut}}(f) = (2.83, 6.01, 5.81)$, $[\text{O}/\text{Fe}] = 0.50$ and $[\text{Zn}/\text{Fe}] = 0.34$.

p	1.157E+01	d	9.904E-16	³ He	2.000E-05	⁴ He	8.755E+00	⁶ Li	8.284E-18
⁷ Li	2.985E-10	⁹ Be	0.000E+00	¹⁰ B	4.046E-16	¹¹ B	2.323E-12	¹² C	1.136E-01
¹³ C	1.958E-08	¹⁴ N	4.340E-05	¹⁵ N	4.765E-05	¹⁶ O	2.119E+00	¹⁷ O	1.400E-07
¹⁸ O	1.152E-04	¹⁹ F	1.921E-06	²⁰ Ne	5.777E-02	²¹ Ne	6.114E-06	²² Ne	6.427E-05
²³ Na	2.285E-04	²⁴ Mg	8.563E-02	²⁵ Mg	2.349E-04	²⁶ Mg	1.961E-04	²⁶ Al	2.037E-05
²⁷ Al	6.201E-04	²⁸ Si	2.406E-01	²⁹ Si	5.870E-04	³⁰ Si	2.531E-04	³¹ P	3.291E-04
³² S	1.575E-01	³³ S	4.397E-04	³⁴ S	2.807E-04	³⁶ S	3.732E-09	³⁵ Cl	4.499E-04
³⁷ Cl	8.097E-05	³⁶ Ar	4.998E-02	³⁸ Ar	1.899E-04	⁴⁰ Ar	6.076E-11	³⁹ K	2.726E-04
⁴⁰ K	6.351E-09	⁴¹ K	1.433E-05	⁴⁰ Ca	1.292E-02	⁴² Ca	5.425E-06	⁴³ Ca	7.554E-07
⁴⁴ Ca	1.674E-04	⁴⁶ Ca	1.666E-11	⁴⁸ Ca	4.226E-12	⁴⁵ Sc	5.962E-07	⁴⁶ Ti	4.129E-06
⁴⁷ Ti	1.076E-05	⁴⁸ Ti	2.311E-04	⁴⁹ Ti	4.454E-06	⁵⁰ Ti	5.385E-11	⁵⁰ V	6.394E-11
⁵¹ V	2.065E-05	⁵⁰ Cr	9.525E-06	⁵² Cr	1.083E-03	⁵³ Cr	3.418E-05	⁵⁴ Cr	6.767E-10
⁵⁵ Mn	3.088E-05	⁵⁴ Fe	2.110E-04	⁵⁶ Fe	8.679E-02	⁵⁷ Fe	1.705E-03	⁵⁸ Fe	1.006E-09
⁵⁹ Co	3.387E-04	⁵⁸ Ni	8.460E-04	⁶⁰ Ni	2.854E-03	⁶¹ Ni	5.241E-05	⁶² Ni	3.304E-05
⁶⁴ Ni	8.406E-11	⁶³ Cu	1.003E-05	⁶⁵ Cu	9.195E-07	⁶⁴ Zn	3.909E-04	⁶⁶ Zn	6.189E-06
⁶⁷ Zn	2.463E-07	⁶⁸ Zn	1.167E-07	⁷⁰ Zn	3.716E-11	⁶⁹ Ga	1.707E-08	⁷¹ Ga	4.113E-10
⁷⁰ Ge	1.906E-08	⁷² Ge	3.417E-10	⁷³ Ge	2.320E-10	⁷⁴ Ge	2.510E-10		

TABLE 13

Yields in the ejecta in M_{\odot} after radio active decay (except ^{26}Al) for the $30M_{\odot} E_{51} = 50$ model shown in Table 4. ($M_{\text{cut}}(i)$, M_{Si} , $M_{\text{cut}}(f) = (2.83, 6.01, 5.81)$, $[\text{O}/\text{Fe}] = 0.50$ and $[\text{Zn}/\text{Fe}] = 0.43$.